Chem

CellPress

Article

A measure of active interfaces in supported catalysts for high-temperature reactions

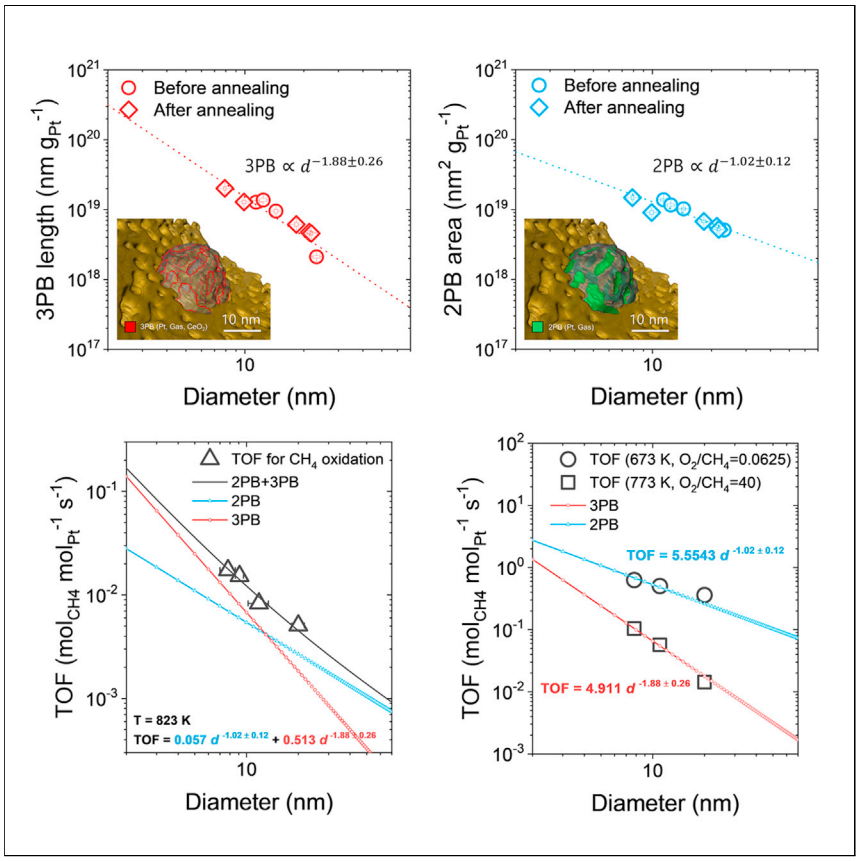

The characterization of the inherent reactivity of the catalyst is critical for the development of an efficient catalytic system for many reactions. Herein, we identify and visualize the active interfaces and quantify the reaction contribution of the individual active site. The analytic methodology suggested in this study enables us to distinguish the importance of individual reaction interfaces depending on the operation conditions (temperature and methane-to-oxygen ratio) and structure of the material (Pt size).

Siwon Lee, Hyunwoo Ha, Kyung Taek Bae, ..., Kang Taek Lee, Hyun You Kim, WooChul Jung

leekt@kaist.ac.kr (K.T.L.)
kimhy@cnu.ac.kr (H.Y.K.)
wcjung@kaist.ac.kr (W.J.)

Highlights

Two different active sites for CH_4 oxidation reaction in Pt/CeO_2 system

Visualization of the active interfaces via 3D electron tomography

Quantification of the reaction contribution for individual active site

Change of key active site depending on the Pt size, temperature and CH_4/O_2 ratio

Lee et al., Chem 8, 1–21
March 10, 2022 © 2021 Elsevier Inc.
https://doi.org/10.1016/j.chempr.2021.11.024

Please cite this article in press as: Lee et al., A measure of active interfaces in supported catalysts for high-temperature reactions, Chem (2021), https://doi.org/10.1016/j.chempr.2021.11.024

Chem

CellPress

Article

A measure of active interfaces in supported catalysts for high-temperature reactions

Siwon Lee,[1,8] Hyunwoo Ha,[2,8] Kyung Taek Bae,[3,8] Seunghyun Kim,[1] Hyuk Choi,[2] Juhyeok Lee,[4] Jun Hyuk Kim,[1] Jongsu Seo,[1] Jin Seok Choi,[5] Yong-Ryun Jo,[6] Bong-Joong Kim,[6] Yongsoo Yang,[4] Kang Taek Lee,[3,7,*] Hyun You Kim,[2,*] and WooChul Jung[1,7,9,*]

SUMMARY

Formulating knowledge of structure-function relationships in heterogeneous catalysis is central to the design of efficient catalysts; yet, the elucidation of dominant reaction sites has remained as a challenge. Here, we present a methodology that can be used to visualize metal-gas and metal-oxide-gas interfaces in three dimensions and to quantify their catalytic activity levels. As a case study, CH_4 oxidation occurring in a Pt/CeO_2 system is chosen. By employing thermally robust $Pt@CeO_2$ model catalysts with size-tunable and monodisperse cores, and gas-permeable shells, we reconstruct a series of structures in 3D via electron tomography and match the information to activity data and theoretical calculations. This strategy reveals that two different interfaces catalyze the CH_4 oxidation and that their contribution to the overall rate changes with the Pt size, temperature, and gas atmosphere. Our results provide an analytic platform on which to explore reaction pathways and mechanisms applicable to multiple reactions and materials.

INTRODUCTION

The interplay between oxide supports and supported metal nanoparticles (NPs) is of high significance in the field of heterogeneous catalysis.[1–5] While the role of oxides was oversimplified in the past, evidence suggests that the use of redox-active oxides (such as CeO_2 and ceria) as a support material can dramatically reshape the landscape of multiple high-value catalytic processes.[6–14] Often, the augmented catalytic activity is attributed to the synergistic interaction between the metal and the support, as the overall rate of reaction can be much greater than the sum of the rates over the support and the metal individually.[15,16] Therefore, many studies, including CO oxidation and water-gas-shift reactions, have been dedicated to unraveling the roles of such interfaces.[17–21] As such, it is implied that the strong local electronic and structural interactions at metal-support interfaces may improve the inherent catalytic activity of supported metal species.[22–24] Other studies have also indicated that such metal-support interactions provide more reactive sites by facilitating interface-mediated reaction paths.[2,8,25,26]

Although the aforementioned studies have produced valuable insights regarding the functions of metal-support interfaces, it should be noted that the overall turnover rate may not be entirely determined by the metal-support interface. In other words, the surfaces of metal particles are still likely to be involved in the bigger picture, even when active supports are used. Generally, for supported metal catalysts, the rate of the overall chemical reaction is primarily determined by the elemental steps that

The bigger picture

Supported catalysts in the form of metal nanoparticles affixed on oxide are at the heart of many chemical industries. However, the information about where the reaction takes place and how much each individual reaction site contributes to the overall rate remains unclear. This work realizes a universal experimental and analysis platform to identify the key reaction sites in a supported catalyst system, which includes the quantification of the turnover rate contribution for individual reaction sites. Thermally robust and geometrically well-defined model catalysts and electron tomography techniques allow three-dimensional visualization of the reaction interfaces, and these data are linked with the catalytic activity and theoretical calculations to quantify the activity of each site. Our work sheds light on the way to explore catalytic pathways and mechanisms for multiple reactions and materials.

Please cite this article in press as: Lee et al., A measure of active interfaces in supported catalysts for high-temperature reactions, Chem (2021), https://doi.org/10.1016/j.chempr.2021.11.024

occur at either the double-phase boundary (2PB) between the gas and the metal or the triple-phase boundary (3PB) at which the gas, metal, and oxide support phases are simultaneously in contact. Indeed, the extent to which each reaction site contributes to the overall reaction rate likely depends on the type of reaction[27] and/or the catalyst composition.[28,29] Furthermore, the dominant reaction site and pathway, even for the same reaction and material, can vary dynamically according to the temperature,[30] ratio of the reactants,[31,32] and the microstructure of the catalyst (i.e., the size distribution of the supported metal NPs).[33,34] To date, however, few studies have attempted to quantify the competition between these two interfaces. Therefore, it has never been possible to answer the following fundamental questions, which can be a substantial cornerstone in the design of an ideal catalyst: "Which of the two interfaces of a given catalyst is more active depending on the reaction, temperature, and gas atmosphere?" and "How exactly is that interface more important than the other, numerically?"

To this end, two major issues must be resolved—first, the density of each active site (i.e., 2PB and 3PB) should be accurately characterized and controlled; thereafter, the catalytic activity of interest should be monitored carefully in relation to the variant ratio of 2PB and 3PB. In this vein, Cargnello et al. successfully determined how the frequency of atoms at 2PB and 3PB varies with the particle size via imaging of the structures of monodispersed metal nanocrystals dispersed on ceria supports. They reported that the change in the CO oxidation rate according to the particle size coincided with the change in the number of atoms at 3PB, which unambiguously demonstrated that the metal-ceria interface is the only active site for CO oxidation in the measurement condition they studied.[35]

Despite the fact that the approach described above represents one of the most triumphant cases of compiling size-activity relationships in heterogeneous catalysis, the temperature window in that study was below the calcination temperature (<573 K), whereas many industrially important chemical reactions proceed at high temperatures (>773 K). Indeed, the coarsening and coalescence of nanosized metal particles are likely to occur at elevated temperatures,[36] posing a particular challenge with regard to maintaining the density of each active site (i.e., the 3PB length and 2PB area per gram of metal used). Methane activation, one of the most treasured reactions for the academy as well as the enterprise, is a typical example of a high-temperature reaction. In particular, this reaction is of interest because specific target applications (i.e., combustion versus reforming) require different operating conditions (i.e., temperatures, types of oxidant, CH_4-to-oxidant ratios) and the corresponding reaction pathways are therefore expected to vary markedly. Cargnello et al. demonstrated that enhanced metal-support interactions can lead to outstanding methane combustion rates in Pd@CeO_2 subunits.[37] Zhang et al. reported that the interfacial site between Co and CeO_2 is essential for the catalytic reaction during the dry reforming of methane.[38] Previous studies have identified the possibility that the metal-ceria interface may play a role in methane activation; yet, no attempt has been made to quantify the roles of 2PB and 3PB sites individually over a wide range of temperatures and gas atmospheres. Therefore, a novel strategy is essential to overcome the morphological evolution of catalysts at high temperatures and thus to assess the value of each key reaction site, which is much more challenging.

In this study, we present thermally stable and oxide-encapsulated metal catalysts with well-defined geometries and reaction sites. Size-tunable monodisperse Pt NPs surrounded by a gas-permeable ceria shell are selected as a model catalyst. For comparison, silica-encapsulated Pt catalysts are prepared as a reference for inert

[1]Department of Materials Science and Engineering, Korea Advanced Institute of Science and Technology (KAIST), Daejeon 34141, Republic of Korea

[2]Department of Materials Science and Engineering, Chungnam National University (CNU), Daejeon 34131, Republic of Korea

[3]Department of Mechanical Engineering, Korea Advanced Institute of Science and Technology (KAIST), Daejeon 34141, Republic of Korea

[4]Department of Physics, Korea Advanced Institute of Science and Technology (KAIST), Daejeon 34141, Republic of Korea

[5]KAIST Analysis Center for Research Advancement (KARA), Korea Advanced Institute of Science and Technology (KAIST), Daejeon 34141, Republic of Korea

[6]School of Materials Science and Engineering, Gwangju Institute of Science and Technology (GIST), Gwangju 61005, Republic of Korea

[7]KAIST Institute for the NanoCentury, Daejeon 34141, Republic of Korea

[8]These authors contributed equally

[9]Lead contact

*Correspondence: leekt@kaist.ac.kr (K.T.L.), kimhy@cnu.ac.kr (H.Y.K.), wcjung@kaist.ac.kr (W.J.)

https://doi.org/10.1016/j.chempr.2021.11.024

Please cite this article in press as: Lee et al., A measure of active interfaces in supported catalysts for high-temperature reactions, Chem (2021), https://doi.org/10.1016/j.chempr.2021.11.024

support. Electron tomography (ET) combined with a three-dimensional (3D) reconstruction method is then utilized to directly observe and quantify the Pt-gas and Pt–CeO_2-gas interfaces. Based on these corresponding results, we measure how the 2PB and 3PB site densities (per gram of Pt) vary with the particle size and how the catalytic activities for CH_4 oxidation change accordingly. The two reaction sites participate simultaneously in CH_4 oxidation, and the contribution of each reaction site to the overall reaction rate is identified, which is further supported by the theoretical interpretation that corroborates the dual-site reaction pathways for methane oxidation in a ceria-Pt system. Our results suggest a reliable platform to explore catalytically active sites and pathways for various chemical reactions, even at high temperatures.

RESULTS AND DISCUSSION

Monodisperse Pt NPs having four different diameters were prepared through aqueous-based colloidal synthesis using a cationic surfactant.[39] Transmission electron microscopy (TEM) bright-field (BF) images show that the particles are 7.8 $\pm$ 0.8, 9.1 $\pm$ 0.5, 11.8 $\pm$ 1.6, and 19.7 $\pm$ 1.7 nm in size, respectively (Figures 1A–1D). Subsequently, the Pt NPs were encapsulated with gas-permeable thin layers of ceria (Figures 1E–1H) or silica (Figures 1I–1L) to prevent coalescence at elevated temperatures. The electrostatic interaction between cationic Pt NPs and anionic Ce precursor complex ions helps cerium oxide shell overcoat Pt NPs uniformly,[40] which is manifested in the energy-dispersive spectroscopy (EDS) mapping (Figure S1). Moreover, scanning electron microscopy (SEM) and TEM BF images at low magnifications confirm that individual Pt NPs are encapsulated in ceria shells (Figure S2). The CeO_2 crystallites in the outer layer of the core-shell structure were ~6 nm in size, corresponding to the calculated value from the X-ray diffraction peaks (Figure S3). The fabricated Pt@CeO_2 structures were later evenly dispersed on additional high-surface area ceria supports (78 m^2 g^{-1}), utilizing the opposite surface charges (Figures S4 and S5). In a similar manner, Pt@SiO_2 samples were prepared by the hydrolysis and condensation of Si precursors around Pt NPs and the subsequent polymerization of silicates, as has been demonstrated elsewhere.[41,42] For all of the samples, we kept the thickness of the ceria and silica shell constant at ~20 and 30 nm, respectively, by adjusting the reaction time so as to eliminate the effects of shell thickness variations on the measured catalytic activities.

These shell configurations demonstrate the capability of effectively inhibiting the structural evolution of the catalysts during high-temperature annealing. Figure 2 shows a series of TEM BF images obtained while annealing a Pt@CeO_2 sample at elevated temperatures (Figures 2A–2D) and at prolonged times (Figures 2D–2F), demonstrating that the Pt@CeO_2 catalysts maintain their morphology without coarsening of Pt NPs up to 873 K. The as-synthesized Pt NPs showed faceted forms due to different growth rates of Pt NP along <100> and <111> directions,[43] but as the temperature increased, the shape of the Pt NPs became spherical with random orientations (Figures S6–S8). The ceria shell also retained its porosity without aggregation. Another important factor to consider is that catalysts can undergo structural evolution on the atomic scale, such as single atom (SA) formation, during a high-temperature heat treatment.[18,44–46] In particular, the Pt–CeO_2 system has been reported to favor the atomic-scale dispersion of Pt during oxidative high-temperature calcination. However, we did not observe any noticeable modifications after calcination at 873 K (Figure S9). Perhaps different catalytic configurations, such as the initial morphology and composition of the catalyst, influenced the process of structural

Please cite this article in press as: Lee et al., A measure of active interfaces in supported catalysts for high-temperature reactions, Chem (2021), https://doi.org/10.1016/j.chempr.2021.11.024

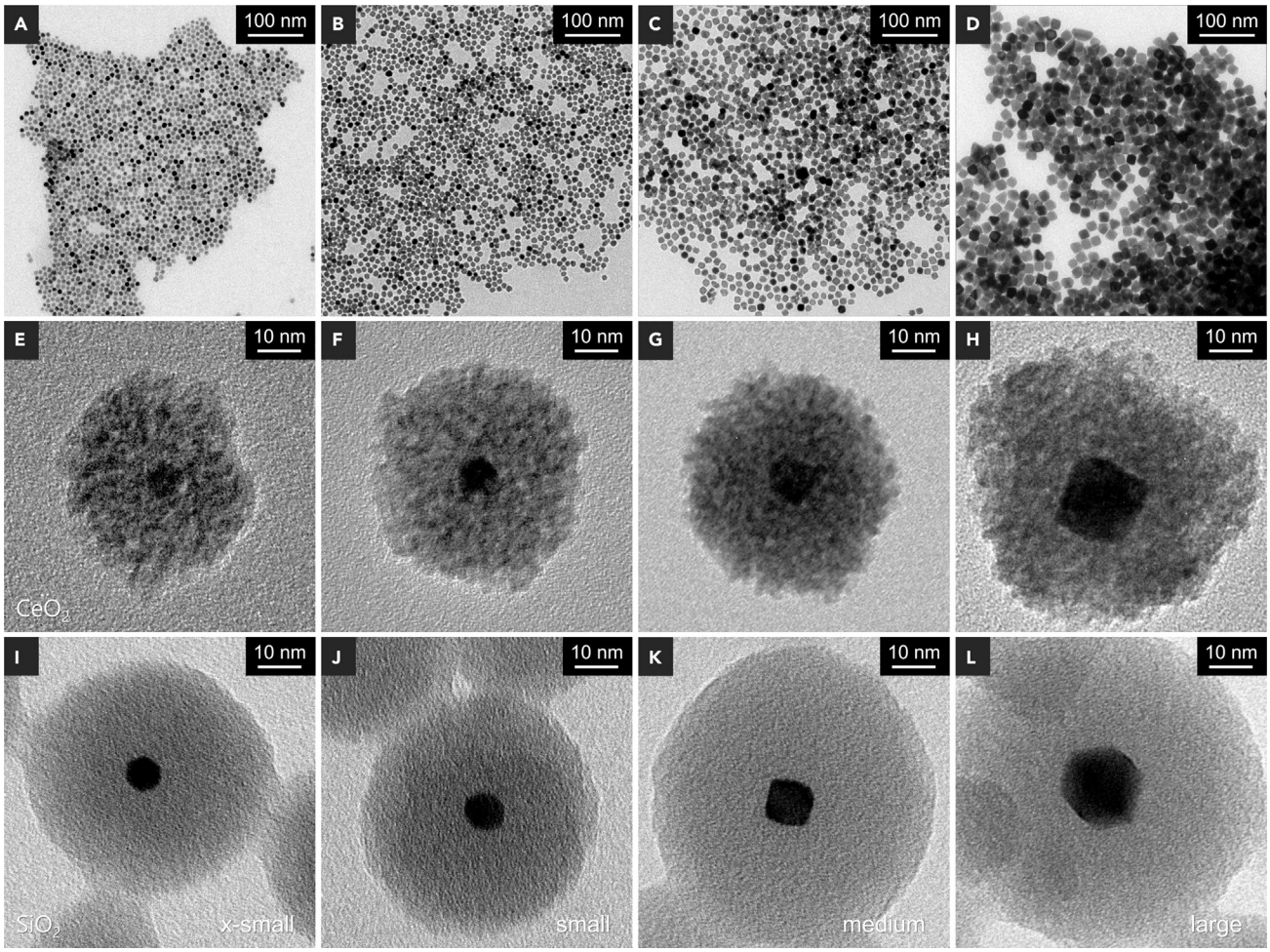

Figure 1. Morphology of as-prepared catalysts

(A–L) TEM images of (A–D) Pt NPs with different particle sizes, (E–H) Pt@CeO_2, and (I–L) Pt@SiO_2 catalysts. Pt NP sizes are referred to as (A, E, and I) x-small, (B, F, and J) small, (C, G, and K) medium, and (D, H, and L) large.

transformation. Similar to Pt@CeO_2, Pt@silica was also stable up to 873 K while maintaining its core-shell structure (Figure S6).

Next, we visualized the Pt@CeO_2 catalysts in three dimensions through ET. For 3D reconstruction, samples before and after a heat treatment at 873 K were utilized, and the cubic voxels of all samples had a side length of 1–2 Å. The 3D resolution of the tomogram was calculated based on the Fourier shell correlation (FSC) with a criterion of 0.143 (Figure S10), showing an average value of 1.28 $\pm$ 0.19 nm. This value is close to the resolution limit (~1 nm) achievable for a 60 nm object at 1° tilt increments based on the Crowther-Klug criterion.[47] We note that in our study, the core-shell catalysts had a size in the range of 50–60 nm, and the tilt increment for tomography data acquisition was 1°. Each resolution for the nine different samples used in this study is summarized in Table S1. The resolution slightly improved after thermal treatment, likely due to the elimination of the residual organic matter. To quantify the microstructural properties in 3D, including the density of the 2PB and 3PB sites, we applied a semi-automated segmentation routine to the tomograms (Figure S11). Figure 3A shows the resultant 3D reconstruction image, indicating that the Pt particle is uniformly surrounded by a mesoporous ceria shell, which is

Please cite this article in press as: Lee et al., A measure of active interfaces in supported catalysts for high-temperature reactions, Chem (2021), https://doi.org/10.1016/j.chempr.2021.11.024

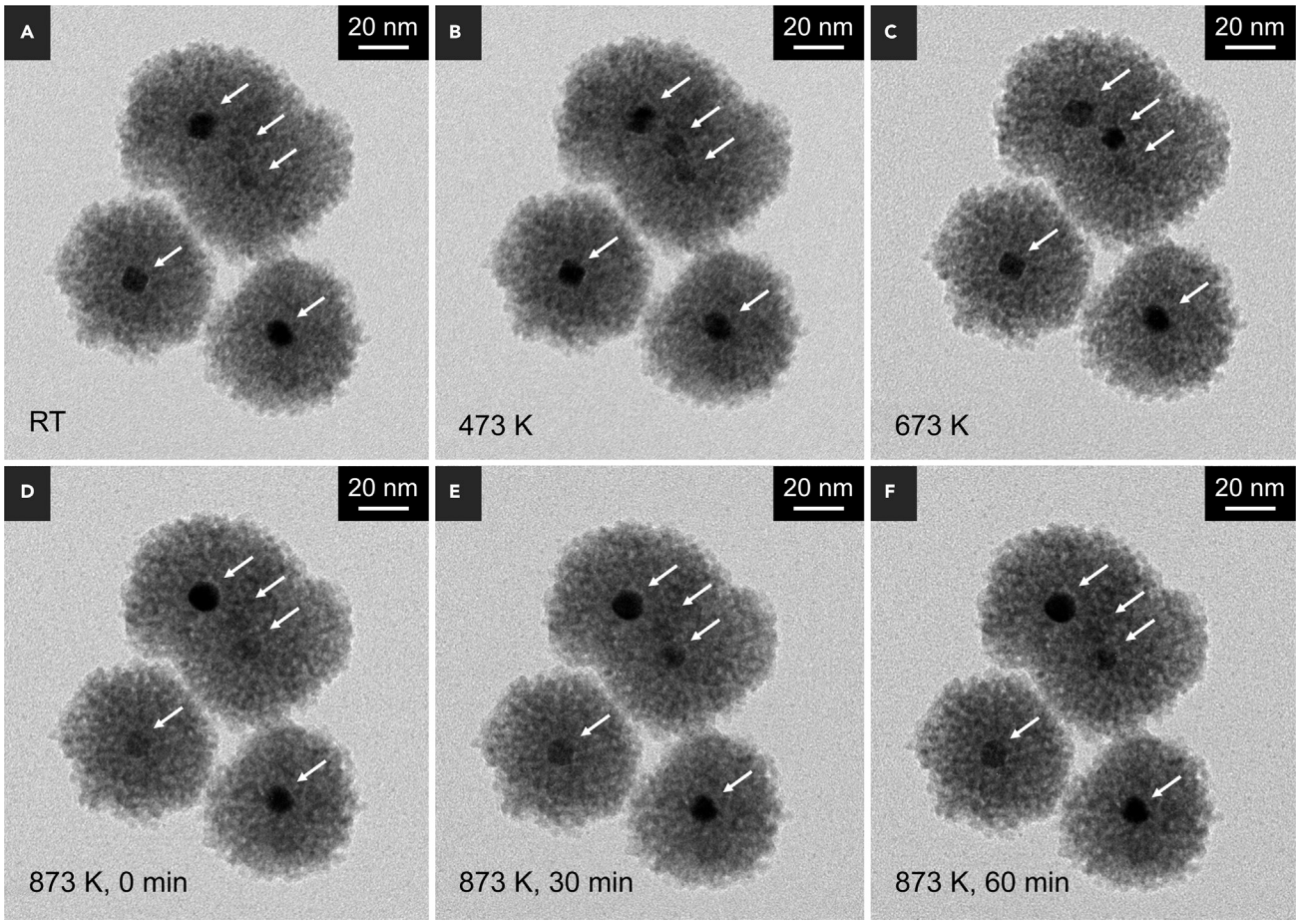

Figure 2. *In situ* heating TEM analyses

(A–F) *In situ* TEM images of the Pt@CeO_2 catalyst under different temperature conditions: (A) room temperature (RT), 298 K, (B) 473 K, (C) 673 K, and (D) 873 K. TEM images of Pt@CeO_2 catalysts after constant-temperature annealing: (E) 30 min and (F) 60 min at 873 K.

readily accessible to gas molecules. A cross-sectional view of the core-shell catalyst along the z axis also shows pores between 1.6 and 3.7 nm in size inside the ceria shell (Figure S12). The accuracy of these pore sizes was confirmed by simulated 3D tomography performed with an image resolution similar to that used in this study (Figure S13). Figures 3B and 3C visually identify the 3PB (red line) and 2PB (green phase) sites, respectively. The 3D tomogram results shown in Video S1 display the morphology and the internal structure of the object, a series of core-shell catalysts, improving our structural understanding of the samples. Table S2 presents quantified results showing how each reaction site density normalized to the Pt loading amount depends on the diameter (d) of the Pt NPs. As the particle size decreases, the density of the 2PB and 3PB sites increases, but different tendencies arise according to the value of d. For example, the density of the two sites in the Pt@CeO_2 composites shows power-law exponents of -1.02 ± 0.12 and -1.88 ± 0.26, respectively, for d (Figures 3D and 3E). Advanced ET technology has recently begun to be applied to heterogeneous catalytic research, but it has only been used to qualitatively confirm the porous structure, and it is noteworthy that this is "the first report" to quantify key reaction sites of nanocomposite catalysts through ET.[48,49] As will be discussed later, the scale relationships between the two reaction site densities with respect to d reflect the respective reaction rates.

Please cite this article in press as: Lee et al., A measure of active interfaces in supported catalysts for high-temperature reactions, Chem (2021), https://doi.org/10.1016/j.chempr.2021.11.024

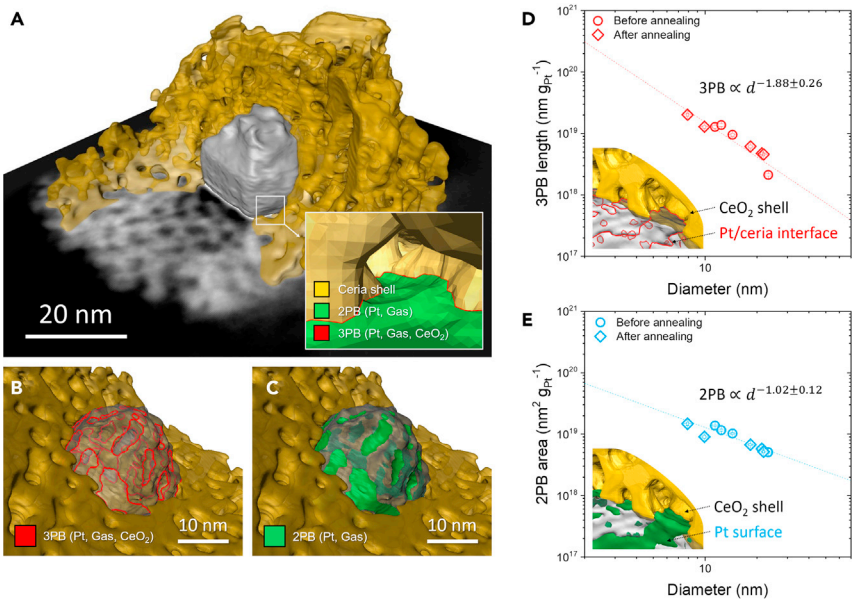

Figure 3. 3D electron tomography

(A) Surface rendered Pt@CeO_2 configuration with a porous ceria shell (yellow) and a Pt NP (gray). The inset image presents a magnified view of the Pt@CeO_2 structure near the interface region between the ceria and Pt. The yellow surface is ceria and the green surface is Pt. The red line indicates the interface site.

(B and C) The cross-section image shows the (B) 3PB (red line) and (C) 2PB (green surface).

(D and E) Variation of (D) the 3PB length and (E) 2PB area per gram of Pt plotted as a function of the Pt NP size. The 3PB length was estimated as the total length of a Pt voxel in contact with ceria. The 2PB area was measured as the total area of a Pt voxel in contact with a pore. Error bars indicate standard errors for estimated particle size, 2PB area, and 3PB length.

Before an in-depth discussion of CH_4 activation on the model catalyst system, the validity of the 3D tomography analysis and the reconstruction process must be ensured; hence, we carried out ad hoc CO chemisorption and oxidation analyses with the Pt@CeO_2 catalysts. First, the 2PB site density was directly measured via CO chemical adsorption, taking into account the property by which CO molecules are selectively adsorbed on the Pt surface. Table S3 shows the exposed metal surface area (EMSA) per unit mass of the Pt@CeO_2 catalysts versus *d*. Thereafter, the 3PB density was reliably deduced by using CO oxidation as a reference reaction. Earlier results demonstrated that the ceria-Pt interface is the dominant reaction site for CO oxidation in the conditions used in this study.[35] Accordingly, the power-law dependence of CO oxidation reactivity on *d* is expected to reflect that of the 3PB interface in our catalytic system. Indeed, the kinetic results of CO oxidation on the Pt@CeO_2 system are identical to those when the ceria-Pt interface is a dominant reaction site in the Pt/CeO_2 system. Moreover, the core-shell catalyst with a high-3PB density has a higher reaction rate than the supported-Pt catalyst, indicating that the 3PB site is an active site (see details in Figures S14 and S15). Figure S16 shows the changes of the 2PB and 3PB site density levels extracted by additional adsorption and oxidation experiments according to the diameter and with power-law exponents for *d* of -0.93 ± 0.02 and -1.95 ± 0.02, respectively. It turns out that the image analyses and experimental supporting results are in good agreement within a standard deviation of 7%. This in combination with the fact that the pore sizes of the ceria shell as judged by tomography are in line with the pore-size distribution obtained via the adsorption experiments clearly demonstrates that our analytic approach is solid.[40] In yet another examination of the

Please cite this article in press as: Lee et al., A measure of active interfaces in supported catalysts for high-temperature reactions, Chem (2021), https://doi.org/10.1016/j.chempr.2021.11.024

validity, we performed additional tomographic experiments using different equipment, thus further ensuring the precision of the linear regression analysis result. As shown in Figure S17, the newly obtained data did not significantly change the slope of the interface variation with particle size. Nonetheless, considering the resolution of 1.28 nm, the issue may arise that tomography may not yield the exact absolute value of the interface near the resolution limit. In this regard, the slope calculation was simulated by assuming that the standard deviation of the particle size and the interface obtained by tomography corresponds to 50% of the mean value. This describes the situation where the standard deviation would increase when the desired information exists near the resolution limit of the tomogram. The results are shown in Figure S18. We obtained slopes of -1.73 ± 0.24 for 3PB and -0.99 ± 0.17 for 2PB, which are similar to the measured slope values. Moreover, still, the slope for 2PB and 3PB indicates quite a large difference. Therefore, even if tomography may not yield the absolute values of the interfaces in some cases, we propose that our approach to distinguish each interface is reliable. In sum, this judicious design of a composite catalyst enables the quantification of idealized 2PB and 3PB interfaces for chemical reactions while effectively suppressing the agglomeration of metal cores at high temperatures; this is of key importance when constructing an analytic platform to find the dominant reaction site for a given catalytic reaction.

Next, we evaluated the activity of CH_4 oxidation on oxide-encapsulated Pt NP catalysts as a case study for typical high-temperature reactions. CH_4 oxidation is a fundamental reaction for various industrial applications, such as catalytic combustion, emission control, and hydrogen reforming,[37,50] but the reaction mechanisms within the ceria-Pt system have not yet been fully identified. The kinetic rate data for CH_4 oxidation over ceria- and silica-encapsulated Pt NPs are shown in Figures 4A and S19. First, the Pt@SiO_2 catalysts used as an inert support reference always exhibit a constant reaction rate regardless of the particle size when normalized to 2PB as determined by CO chemisorption (Figure S19). In contrast, the Pt encapsulated with a reducible CeO_2 support (Pt@CeO_2) exhibited directly opposite behavior, as the reaction rate strongly depends on the particle size (Figure 4A). This implies that, in addition to the Pt surface, another reaction site, plausibly the ceria-Pt interface, acts as a reaction area in the ceria-Pt system. Because the increase in the 3PB density is more pronounced than that of the 2PB density as the size of the Pt dwindles, it is anticipated that the role of the 3PB site is emphasized with tiny Pt NPs. Indeed, as the Pt size decreases, the apparent values of E_a gradually decrease from 82.8 to 63.8 kJ mol^{-1}, signifying that the dominant active site adapts with the catalyst size.

Reaction orders for CH_4 and O_2 will present a clearer understanding of the role of the Pt–ceria interface in CH_4 oxidation reactions. For silica-based catalysts, an increase in the partial pressure of methane (pCH_4) accelerates the reaction, whereas an increase in the partial pressure of O_2 (pO_2) slows down the reaction, with reaction order values of 0.95 and −0.40, respectively, for CH_4 and O_2 (Figure S20). These reaction order values are in good agreement with the reported values, meaning that the Langmuir-Hinshelwood-type of reaction path represents the surface reaction between adsorbed CH_4 and O_2 on Pt sites.[51,52] In the ceria-based sample, however, a relatively weak dependence of the reaction rate to pCH_4 and pO_2 was noted, with corresponding reaction orders of 0.55 in CH_4 and −0.19 in O_2; thus, it is obvious that methane combustion occurs through a reaction pathway different from that associated with silica-based catalysts. Similarly, a less sensitive dependency of the catalytic activity on the partial pressure of the reactants was observed in the ethane, propane, and butane oxidation reactions on ceria-supported noble metal

Please cite this article in press as: Lee et al., A measure of active interfaces in supported catalysts for high-temperature reactions, Chem (2021), https://doi.org/10.1016/j.chempr.2021.11.024

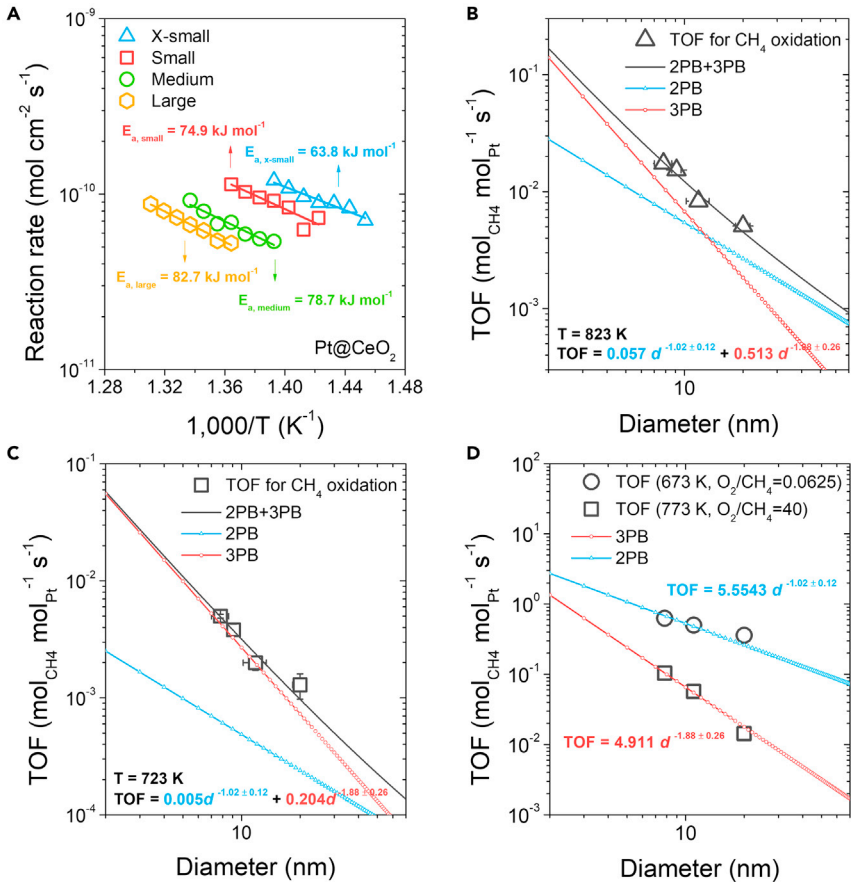

Figure 4. Size-dependent activities

(A) Arrhenius-type plot of CH_4 oxidation over CeO_2-encapsulated Pt catalysts. Reaction rates are normalized by the EMSA as identified from a CO chemisorption analysis.

(B and C) TOF values of Pt@CeO_2 catalysts for CH_4 oxidation measured at (B) 823 K (black open triangle symbols) and (C) 723 K (black open square symbols). TOF values were fitted to the solid black line. The blue line with open triangle symbols and the red line with open circle symbols represent the size-dependent density levels of the 2PB and 3PB, respectively. The O_2/CH_4 ratio of the input gas is 4.

(D) TOF values of CH_4 oxidation catalyzed by Pt@CeO_2 at an O_2/CH_4 ratio of 0.0625 at 673 K (black open circle symbols) and an O_2/CH_4 ratio of 40 at 773 K (black open square symbols). Error bars indicate standard errors for particle sizes and TOFs.

catalysts.[52] Given the ability of ceria as an oxygen reservoir, these results can be explained by the dual-function mechanism in which the ceria supplies oxygen to the supported metal and the delivered oxygen interacts with methane provided near the Pt–ceria interface.[52,53] The presence of Pt indeed activates lattice oxygen atoms in the vicinity of the ceria surface and reduces the activation energy for the dissociative adsorption of methane.[26,54] Thus, the aforementioned results consistently represent the principal evidence of the active role of Pt–ceria interfacial sites regarding CH_4 oxidation, while their degree of participation may vary with the particle size.

The values of the turnover rate as a function of the catalyst diameter can be considered as more direct and decisive evidence specifying the predominant interface, whereas the plot can be further deconvoluted to quantify the accurate ratio of reaction engagement between 2PB and 3PB. The overall reaction rate comes from

Please cite this article in press as: Lee et al., A measure of active interfaces in supported catalysts for high-temperature reactions, Chem (2021), https://doi.org/10.1016/j.chempr.2021.11.024

scaling relationships for CH_4 oxidation, described in the form of a double-logarithmic plot (log TOF versus log *d*). For the Pt@silica samples, we found that the turnover frequencies (TOFs) for CH_4 oxidation were proportional to $d^{-0.51\pm0.36}$, which is consistent with the trend of EMSA, which varies with *d* (EMSA $\propto d^{-0.54\pm0.18}$) (Figure S21). This observation corroborates the contention that CH_4 combustion occurs dominantly at the Pt surface sites of the Pt@silica catalysts, which is further supported by the fact that the reaction rate normalized by EMSA is independent of *d* (Figure S19). In contrast, the tendency of the change in the TOF in the Pt@ceria samples is not always consistent with the trend of the 2PB site density variation according to the value of *d* (Figure 4B); rather, the power-law dependence of *d* for TOF exists between those of 2PB and 3PB. Therefore, the TOF values of CH_4 oxidation could be fitted using two parallel relationships, as plotted in Figures 4B–4D, showing the TOF value versus *d* (i.e., TOF $\propto C_1 d^{-1.02} + C_2 d^{-1.88}$, where C_1 and C_2 are constant). These data fitting results reveal that both active sites concurrently contribute to the methane oxidation reaction and allocate their proportion under the given reaction condition. For example, as shown in Figure 4B and Table S4, when *d* is 10 nm, the reaction temperature is set to 823 K, and the O_2/CH_4 ratio of the input gas is 4, it can be found that 2PB and 3PB are almost equally important and partake in the overall reactivity at rates of 45% and 55%, respectively.

Based on these scaling relation results, we can quantify how each interface contributes to the overall TOF value according to the Pt particle size, temperature, and gas composition (ratio between CH_4 and O_2). In terms of *d*, the smaller the particle size, the greater the number of sites at the Pt/ceria interface relative to the surface area of Pt exposed at a given mass, meaning that the overall reactivity of the core-shell catalysts is determined more by an elemental process at 3PB. On the other hand, for larger NPs, 2PB dominates the overall reaction. As shown in Table S4, the role of 3PB increases rapidly from 15% to 90% as the size of Pt decreases from 100 to 1 nm at 823 K with an O_2/CH_4 ratio of 4. In addition, because the elemental steps in 2PB and 3PB have different activation energies (~100 and ~60 kJ mol^{-1}, respectively), the contribution of each interface varies with the temperature. For example, the 3PB interface plays a more dominant role at the lower temperature of 723 K as compared with the role at 823 K if all other factors (e.g., the feed gas ratio and Pt NP size) are equal (Figures 4B and 4C; Tables S4 and S5). With smaller Pt particles, as shown in Figures S22 and S23, we can again confirm the rationality of our results, explaining the role of 2PB and 3PB sites. These results indicate that the metal-ceria interface density must be maximized to achieve CH_4 activation at lower temperatures, consistent with earlier findings in the literature.[28,55]

In addition to the particle size and temperature effects, the dominant active region also varies with the gas composition introduced. As shown in Figure 4D, if the reaction occurs at an O_2/CH_4 ratio of 0.0625 (oxygen-lean condition), 2PB contributes entirely to the overall TOF values. In contrast, 3PB dominates the overall catalytic activity at a higher O_2/CH_4 ratio of 40 (oxygen-rich condition). These reactant-gas-dependent catalytic responses arise from the difference in the predominantly adsorbed species on the Pt NPs depending on the O_2/CH_4 ratio.[56] At higher relative oxygen ratios, more oxygen covers the Pt surface, with intimate Pt–O interactions. The preferred oxygen saturation may suppress CH_4 adsorption on the Pt surface and thus the participation of 2PB accordingly. This reduces the overall activity (Figure S24); however, it makes the participation of 3PB relatively important. Methane oxidation at 2PB, on the other hand, plays an important role during oxygen-lean conditions. Eventually, combining the robust model catalytic system and a quantitative

Please cite this article in press as: Lee et al., A measure of active interfaces in supported catalysts for high-temperature reactions, Chem (2021), https://doi.org/10.1016/j.chempr.2021.11.024

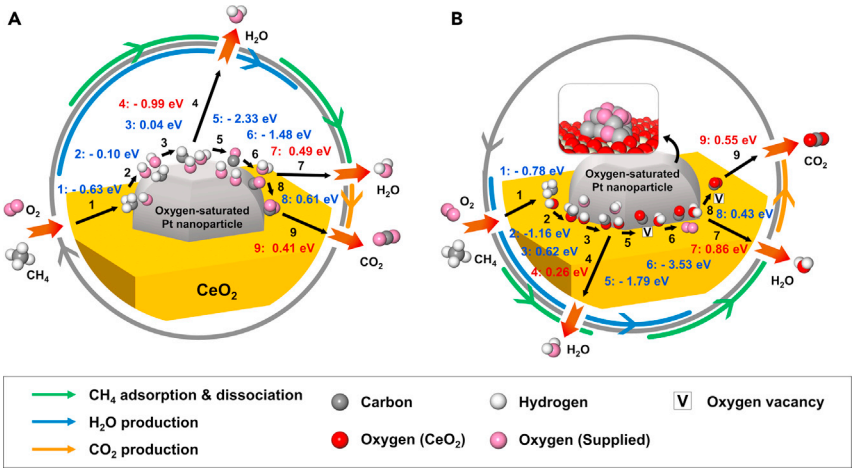

Figure 5. DFT-estimated CH_4 oxidation pathways

(A and B) Schematic DFT-estimated CH_4 oxidation pathways catalyzed by (A) the 2PB and (B) the 3PB of Pt@CeO_2. Numbered black arrows denote the individual reaction steps of CH_4 oxidation. Corresponding reaction energy values are presented. Sequential 2PB reaction involves (A1) dissociative CH_4 adsorption, (A2) CH_3 dissociation, (A3) CH_2 dissociation and H_2O formation, (A4) 1st H_2O production (desorption), (A5) CH dissociation and CO formation, (A6) H_2O formation, (A7) 2nd H_2O production (desorption), (A8) CO_2 formation, and (A9) CO_2 production (desorption) pathways. In comparison, the 3PB reaction pathway consists of (B1) dissociative CH_4 adsorption, (B2) CH_3 dissociation, (B3) CH_2 dissociation and H_2O formation, (B4) 1st H_2O production (desorption), (B5) CH dissociation, CO and H_2O formation, (B6) vacancy healing, (B7) 2nd H_2O production (desorption), (B8) CO_2 formation, and (B9) CO_2 production (desorption). Refer to Figures S26 and S27 for full reaction pathways and energetics.

analysis of nanoscale interfaces, we directly observed the dual-site reaction mechanism toward high-temperature CH_4 oxidation under various reaction conditions.

To clarify the mechanistic details pertaining to the roles of 2PB and 3PB, we performed DFT calculations. Two types of structural models are utilized to model CH_4 oxidation on core-shell Pt@CeO_2 comprehensively: a conventional Pt_9 NP on CeO_2(100) and an inverse Ce_7O_{14} NP on Pt(111). Here, only the energetics from the former system is presented because relatively consistent results were deduced from both systems (refer to supplemental information for additional data pertaining to the latter model). The calculated binding energy, E_{bind}, of CH_4 (−0.44 eV) and O_2 (−2.14 eV) molecules on Pt NPs indicates that the Pt NP preferentially binds to O_2 initially (Figure S25). Because subsequent dissociation of the Pt-bound O_2 molecule is exothermic with a low E_a, we initially saturated the Pt NPs of Pt@CeO_2 models with oxygen (Figure S25). Later, the O-saturated Pt NP dissociatively adsorbs a CH_4 molecule in the presence of the pre-adsorbed oxygen atoms (Figures 5A1 and 5B1), initiating the subsequent CH_4 oxidation steps. Although both the Pt–CeO_2 interface (3PB) and the surface Pt (2PB) can bind to CH_4, 3PB is energetically more preferred (Figure 5). Moreover, 3PB provides a greater thermodynamic driving force for the sequential dehydrogenation of CH_4 (Figure 5), suggesting that 3PB is the primary CH_4 activation site at low CH_4 concentrations. Interestingly, both 2PB and 3PB sites show high E_a values for the dehydrogenation of CH_4 (Figures S26 and S27). However, considering that the reaction occurs at a high temperature and that the entropic contribution to the energetics of CH_4 dissociation provides an additional driving force for hydrogen abstraction overall, these E_a values will not hinder the reaction. The DFT-estimated subsequent dissociative adsorption of CH_4 and the dehydrogenation of CH_3* (Figure 5) show that Pt-bound oxygen atoms, Pt–O*, accept the

Please cite this article in press as: Lee et al., A measure of active interfaces in supported catalysts for high-temperature reactions, Chem (2021), https://doi.org/10.1016/j.chempr.2021.11.024

abstracted hydrogen atoms from CH_4 and release them as H_2O (see Figures S26 and S27 for more details). The formation and release of the first H_2O molecule on the 2PB and 3PB sites proceed rapidly (Figures 5A3, 5A4, 5B3, and 5B4). Although the release of the second H_2O from 2PB or 3PB requires an E_{de} value of 0.49 or 0.86 eV, respectively (Figures 5A7 and 5B7), a large portion of E_{de} can be supplied by the positive (qualitatively) entropic contribution to the Gibbs free energy of H_2O desorption.

The remaining C of CH_4 was combined with two different oxygen species: Pt–O* (2PB) or lattice oxygen of CeO_2 (3PB), being transformed into Pt–CO* (Figures 5A5 and 5B5). These two oxygen species concurrently contribute to the overall CO_2 production rate because their E_a values of CO_2 formation are nearly identical (Figures S26 and S27). The comparable E_{de} values of CO_2 from 2PB (0.41 eV) and 3PB (0.55 eV) predict that both are energetically available (Figures 5A9 and 5B9). Supporting our experimental prediction that Pt@ceria provides at least two active sites for CH_4 oxidation, the DFT calculation results describe the dual-site reaction pathways in a condition in which O_2 covers the Pt surface, similar to the actual environment. Because no notable relative superiority of a specific site was found, the relative ratio of 2PB and 3PB, a direct function of the size of the Pt NPs, steers the dominant reactive species and the pathway for CH_4 oxidation.

In summary, we showcased a generalizable empirical and characterization framework with which to determine the dominant reaction sites in the Pt–CeO_2 system with regard to methane oxidation, a crucial reaction proceeding at elevated temperatures. In contrast to recent reports that narrowly focused on the roles of redox-active supports, we found that the primary reaction sites between 2PB and 3PB vary with extreme sensitivity according to the temperature, gas pressure, and the size of the metal NPs. In particular, empowered by a combination of a theory-based mechanistic study and state-of-the-art experimental synthesis and analysis, we revealed that a larger NP size, an increasing T value, and a decreasing pO_2 value lead to a greater contribution of 2PB to the total methane turnover rate, and vice versa, marking, "for the first time," the development of a quantitative direct relationship between the areal fraction of the reaction sites and the catalytic activity of metal NPs toward high-temperature chemical reactions. The aforementioned strategy may globally guide other metal-catalyst support systems for a variety of industrially important reactions, and the insights gained here present a roadmap with which to find the "ideal catalyst" for a specific target condition.

EXPERIMENTAL PROCEDURES

Resource availability

Lead contact

Further information and requests for resources should be directed to and will be fulfilled by the lead contact, WooChul Jung (wcjung@kaist.ac.kr).

Materials availability

All unique/stable reagents generated in this study are available from the lead contact with a completed materials transfer agreement.

Data and code availability

All data reported in this paper will be shared by the lead contact upon request. This paper does not report original code.

Please cite this article in press as: Lee et al., A measure of active interfaces in supported catalysts for high-temperature reactions, Chem (2021), https://doi.org/10.1016/j.chempr.2021.11.024

Synthesis of Pt nanoparticles

An aqueous solution of potassium tetrachloroplatinate(II) (10 mM and 5 mL) and alkyltrimethylammonium bromide (C_nTAB, n = 12, 14, 16, and 18) (400 mM and 12.5 mL) was added to 29.5 mL of deionized (DI) water while being stirred. The mixture was then heated to 323 K for 20 min. When using the C_{18}TAB surfactant, the mixture was heated to 328 K for 25 min due to its greater hydrophobicity. Subsequently, a reduction agent, sodium borohydride (500 mM and 3 mL), was injected into the mixture. Hydrogen gas formed in the flask was released into the fume hood for 20 min using a syringe needle. The mixture solution was then aged at 323 K for 15 h under magnetic stirring. The mixture, including the C_{18}TAB surfactant, was aged at 328 K for 15 h. Afterward, the resulting solution was centrifuged at an appropriate rpm to clean up the as-synthesized Pt NPs. For the Pt NPs capped by C_{18}TAB (i.e., x-small-sized Pt), 10 mL of ethanol was added to the resulting solution, and the mixture was then centrifuged at 12,000 rpm for 60 min. After removing the supernatant, a volume of DI water equal to that of the removed supernatant was added and this was centrifuged again at 12,000 rpm for 60 min. For the Pt NPs capped by C_{16}TAB (i.e., small-sized Pt), the resulting solution was subjected to centrifugation at 3,000 rpm for 30 min. Then, the supernatant was mixed with 10 mL of ethanol, after which centrifugation took place at 12,000 rpm for 30 min. For the Pt NPs capped by C_{14}TAB (i.e., medium-sized Pt), the resulting solution was subjected to centrifugation at 3,000 rpm for 30 min. Subsequently, the supernatant was separated and centrifuged again at 12,000 rpm for 15 min twice. For the Pt NPs capped by C_{12}TAB (i.e., large-sized Pt), the resulting solution was centrifuged at 6,000 rpm for 15 min. The precipitate at the bottom of the centrifuge tube was collected and dispersed in DI water (5 mL) for further use.

Synthesis of Pt@CeO_2 nanostructures

The as-synthesized C_nTAB (n = 12, 14, 16, and 18)-capped Pt NPs at a level of 0.5 mL were blended with an aqueous solution of C_{14}TAB (25 mM and 40 mL). For the C_{12}TAB-capped Pt NPs, 0.75 mL of a colloidal solution of Pt NPs was used. The Pt concentration of each solution is compiled in Table S3. To cover the surface of the Pt NPs with a precursor containing Ce ions, aqueous solutions of EDTA-NH_3 and $Ce(NO_3)_3 \cdot 6H_2O$ were prepared, as follows. For the preparation of the EDTA-NH_3 solution, concentrated ammonia (0.38 mL and 28–30 wt %) was mixed with an aqueous solution of EDTA (10 mM and 40 mL). An aqueous solution of $Ce(NO_3)_3 \cdot 6H_2O$ (100 mM and 10 mL) was prepared by dissolving the $Ce(NO_3)_3 \cdot 6H_2O$ precursor in DI water, after which 3 mL of EDTA-NH_3 and 0.3 mL of $Ce(NO_3)_3 \cdot 6H_2O$ solutions were injected into the mixture solution of Pt and C_{14}TAB. After shaking the mixture gently for 1 min, it was thermally aged at 363 K for 8 h. The resulting cloudy brown solution was subjected to centrifugation at 8,000 rpm for 10 min, and the final precipitate was collected and dispersed in DI water (10 mL) for further use.

Synthesis of Pt@silica nanostructures

The as-synthesized C_nTAB (n = 12, 14, 16, and 18)-capped Pt NPs at a level of 0.5 mL were dispersed in an aqueous solution of C_{14}TAB (10 mM and 40 mL for x-small, small, and medium-sized Pt NPs; 12.5 mM and 40 mL for large-sized Pt NPs). To the C_{14}TAB-stabilized Pt NPs solution, concentrated ammonia (0.1 mL and 28–30 wt %) was added to keep the pH level at 10–11. In order to form a silicon oxide shell around the dispersed Pt NPs, 10 vol % of TEOS diluted with ethanol (3 mL for x-small and small, 4 mL for medium, and 5 mL for large Pt NPs) was added. The mixture was left under stirring for 1 h to allow oxide encapsulation to occur. The resulting cloudy

Please cite this article in press as: Lee et al., A measure of active interfaces in supported catalysts for high-temperature reactions, Chem (2021), https://doi.org/10.1016/j.chempr.2021.11.024

brown solution was centrifuged at 12,000 rpm for 15 min, and the final precipitate was collected and dispersed in DI water (1 mL) for further use.

Preparation of the Pt(1 wt %)@CeO_2/CeO_2 catalysts

A suitable amount of CeO_2 support was dispersed in a basic solution to prepare the surface of CeO_2 to have a negative charge. The cerium oxide support was prepared by the calcination of $Ce(NO_3)_3 \cdot 6H_2O$ in air at 723 K for 20 h. Based on the ICP-OES results shown in Table S3, we prepared an appropriate amount of a Pt@CeO_2 synthetic solution so that the amount of Pt was adjusted to 1 wt % to the total weight of the catalyst. Then, a concentrated ammonia solution (0.38 mL, 28–30 wt %) was added to make the surface of the core-shell structure negative. C_{14}TAB (10 mM) was added to the Pt@CeO_2 solution so that the surface charge of the core-shell structure would be positive (Figure S4; Table S6). Each mixture solution (CeO_2 support and Pt@CeO_2) was mixed together with stirring at 300 rpm for 10 min. The resulting solution was centrifuged at 8,000 rpm for 10 min and the precipitate was collected and dried at 353 K overnight. The as-synthesized Pt(1 wt %)@CeO_2/CeO_2 catalyst was calcined at 623 K for 5 h in air to eliminate the residual organics, such as C_nTAB, EDTA, and ethanol, and to lead to the formation of pores in the cerium oxide shell. The wt % of Pt NPs in the final catalysts was reconfirmed by means of an X-ray fluorescence (XRF) analysis. The surface charge of each species was verified via a zeta-potential measurement. The zeta-potential measurement and XRF results are compiled in Tables S6 and S7, respectively.

Preparation of the Pt(1 wt %)/CeO_2 catalysts

A suitable amount of CeO_2 support was dispersed in a basic solution to prepare the surface of CeO_2 to impart a negative charge. We then prepared a proper amount of a colloidal solution consisting of positively charged Pt NPs so as to adjust the amount of Pt to 1 wt % of the total weight of the catalyst (the Pt concentration was verified by ICP-OES and is compiled in Table S3). Each solution (CeO_2 support and Pt NPs) was mixed by stirring at 300 rpm for 10 min. The resulting solution was then centrifuged at 8,000 rpm for 10 min and the precipitate was collected and dried at 353 K overnight. The as-synthesized Pt(1 wt %)/CeO_2 catalyst was calcined at 623 K for 5 h in air. The wt % of the Pt NPs in the final catalysts was confirmed by an XRF analysis (Table S7).

Preparation of the Pt(1 wt %)@silica/silica catalysts

A suitable amount of silicon oxide support was dispersed in a basic solution to prepare the surface of silica to have a negative charge. Based on the ICP-OES results shown in Table S3, we prepared an appropriate amount of a positively charged Pt@silica synthetic solution so that the amount of Pt was adjusted to 1 wt % of the total weight of the catalyst. Each solution (silica support and Pt@silica) was mixed while being stirred at 500 rpm for 30 min. Afterward, the mixture was separated into the supernatant liquid and the precipitate. The supernatant liquid was removed, and the precipitate was dried at 353 K overnight. The as-synthesized Pt(1 wt %)@silica/silica catalyst was calcined at 723 K for 3 h in air to remove the residual organics, such as C_nTAB, TEOS, and ethanol, leading to the formation of pores in the silica shell.

Preparation of the 2.8 nm-Pt@CeO_2/CeO_2 catalyst

To prepare the Pt NPs (ca. 2.8 nm), 200 mg of platinum(II) acetylacetonate were mixed in 1-octadecene (10 mL) together with oleylamine (OLAM, 1 mL) and oleic acide (OLAC, 1 mL) in a three-neck round bottom flask. The flask with the mixture was connected to the standard Schlenk line. The mixture solution was heated to

Please cite this article in press as: Lee et al., A measure of active interfaces in supported catalysts for high-temperature reactions, Chem (2021), https://doi.org/10.1016/j.chempr.2021.11.024

393 K in 20 min and flushed at 393 K for 15 min under Ar flow. Next, the solution was left under Ar flowing for 30 min to remove water and other impurities. Subsequently, the solution was further heated to 473 K at a ramping rate of 4 K min^{-1}. After the reaction at 473 K for 30 min, the mixture solution was cooled down to RT. The stirring rate was kept at 500 rpm during the synthesis procedure. The as-synthesized Pt NPs were separated by centrifugation twice at 8,000 rpm for 10 min. The Pt NPs were dispersed in toluene with 50 μL of OLAM for further use. For the preparation of the 2.8 nm-Pt/CeO_2, the Pt NPs dispersion was mixed with a solution of CeO_2 dispersed in 40 mL of toluene. The mixture was left stirring at 300 rpm for 10 min. Next, the mixture was separated by centrifugation at 5,000 rpm for 10 min. The precipitates were dried in an oven at 353 K overnight. The as-synthesized 2.8 nm-Pt/CeO_2 was calcined at 623 K for 5 h in air to remove the remaining organics. To cover the Pt NPs by CeO_2 shell, the 2.8 nm-Pt/CeO_2 powder was immersed in 40 mL of DI water. After then, cerium nitrate hexahydrate ($Ce(NO_3)_3 \cdot 6H_2O$, 1 mM) and hexamethylenetetramine (HMTA, 10 mM) were added into the solution. The mixture was heated to 343 K for 30 min to oxidize cerium precursors on the surface of Pt NPs. The as-synthesized 2.8 nm-Pt@CeO_2/CeO_2 catalyst was rinsed in DI water, dried in an oven at 353 K overnight, and calcined at 623 K for 5 h.

Catalytic activity tests (CH_4 and CO oxidation)

A fixed-bed micro-reactor with a 4 mm inner diameter was used to measure the catalytic activity of the CH_4 and CO oxidation processes. To create the catalyst bed, 50 mg of a catalyst was mixed with 100 mg of quartz sand, and this was then placed between layers of quartz wool. To ensure that neither mass nor heat transfer limitations affected the measured results, we performed the conversion while changing the flow rate at a constant space velocity, finding that the conversion characteristics remained constant (Figure S28). The feeds for CH_4 oxidation (composed of 0.5 vol %-CH_4 and 2 vol %-O_2 in an Ar balance) and CO oxidation (composed of 1 vol %-CO and 4 vol %-O_2 in an Ar balance) were passed through the reactor. To investigate the effect of the feed gas ratio, we adjusted the input gas ratio (O_2/CH_4) from 0.0625 (oxygen-lean condition) to 40 (oxygen-rich condition). The total flow rate was 50 mL min^{-1} for both oxidation reactions. The reaction rate was recorded while increasing the temperature with a ramping rate of 3 K min^{-1}. For each test, the catalyst was activated in the reaction environment at 873 K for CH_4 oxidation and 573 K for CO oxidation. The gas concentration change was detected with a quadrupole mass spectrometer (Pfeiffer Vacuum GSD320) in real time. The CH_4 and CO conversion ratios (%) were defined as the ratio of the converted reactant to the total input reactant (i.e., CH_4 conversion ratio = $100 \times (mol_{CH4,\ inlet} - mol_{CH4,\ outlet})/mol_{CH4,\ inlet}$; CO conversion ratio = $100 \times (mol_{CO,\ inlet} - mol_{CO,\ outlet})/mol_{CO,\ in}$). To rule out the effect of the CeO_2 support itself toward CH_4 oxidation, we subtracted the reaction rate of the CeO_2 support from the overall measured reaction rate so as to determine the reaction rate associated with Pt NPs. The reaction orders for CH_4 and O_2 were determined as follows. For the reaction order of CH_4, the reaction rate was measured by varying the pCH_4 (from 2×10^{-3} to 6×10^{-3} atm) while keeping the pO_2 constant at 5×10^{-2} atm. In the same way, for the reaction order of O_2, we determined the reaction rate according to the change in pO_2 (from 1×10^{-2} to 5×10^{-2} atm) while keeping the pCH_4 constant at 2×10^{-3} atm. To investigate the reaction order of CO and O_2, we measured the reaction rate by changing the partial pressure of carbon monoxide (pCO) (from 1×10^{-3} to 6×10^{-3} atm) while holding the pO_2 level at 5×10^{-2} atm. We also carried out rate measurements according to the pO_2 variation while keeping the pCO level at 1×10^{-3} atm. Methane gas was detected by the m/z = 15 peak instead of the 16 peak to avoid interference from the fragments

Please cite this article in press as: Lee et al., A measure of active interfaces in supported catalysts for high-temperature reactions, Chem (2021), https://doi.org/10.1016/j.chempr.2021.11.024

of CO, CO_2, H_2O, and O_2. The CO gas signal was measured by taking into account the contribution from CO_2 gas via the mass concentration determination (MCD) mode.

Characterization techniques

The morphologies and elemental compositions of the synthesized core-shell catalysts were characterized by means of bright-field TEM and energy-dispersive X-ray spectroscopy (EDX) (JEOL JEM-3010 operating at 300 kV and FEI Talos F200X operating at 200 kV), respectively. Catalyst powder samples were drop casted onto lacey carbon films on copper grids (Electron Microscopy Sciences) from concentrated ethanol and then dried in an oven at 343 K for 10 min. For *in situ* heating TEM observations, we used an *in situ* heating holder (Gatan 652 double tilt) with a TEM (FEI Tecnai G2 F30 S-Twin and JEOL JEM-3011 HR) operating at 300 kV. For the acquisition of the ET series, we used a tomography holder (Fischion Model 2020 Advanced Tomography Holder) with a TEM (FEI Talos F200X) operating at 200 kV and an aberration-corrected TEM (FEI Titan Cubed G2 60-300) operating at 300 kV. Before the sample loading, we sufficiently cleaned and dispersed each sample in the ultrasonicator for 30 min. Next, a very small amount of sample suspension (1 μL) was drop casted onto a silicon nitride (SiN) membrane with 0.5 × 1.5 mm^2 aperture on 200 μm silicon (Ted Pella) using a micropipette, and then dried in a vacuum chamber (75 Torr) at 323 K overnight. Thereafter, the as-prepared sample was mounted in an ultra-high vacuum (UHV) chamber overnight before the image acquisition for tomography to remove residual organics. A pre-heat treatment of the catalyst for ET was carried out using an *in situ* heating TEM (FEI Tecnai G2 F30 S-Twin). SEM images were acquired using a Hitachi S-4800 device. The Pt NP concentrations in the solutions and the Pt/Ce molar ratios of the core-shell particles were determined by an inductively coupled plasma mass spectrometer (Agilent ICP-OES 720) and an XRF spectrometer (Rigaku ZSX Primus II). For ICP-OES, samples were dissolved in aqua regia and diluted prior to the measurement. The average particle size was calculated by counting more than 200 individual particles. The surface charge of the samples was characterized using a zeta-potential analyzer (Otsukael ELS-Z2). The crystal structure of the samples was identified by powder X-ray diffraction using a Rigaku D/Mas-2500 device with Cu-Kα radiation at 40 kV and 200 mA with a scan rate of 4° per minute from 20° to 60°. CO chemisorption experiments were conducted on a Micromeritics ASAP 2020. The samples were placed in a U-shaped quartz reactor, heated under flowing O_2 (5%) in helium at 723 K for 1 h, reduced in flowing H_2 (5%) in helium at 423 K for 1 h, and then evacuated at 573 K for 4 h. CO chemisorption experiments performed at RT. Nitrogen adsorption/desorption isotherms were carried out at the temperature of liquid nitrogen (77 K) using a Micromeritics Tristar II 3020 instrument to identify the pore-size distribution, pore volume, and total surface area of the samples.

Electron tomography

The tomographic tilt series were acquired in high-angle annular dark-field scanning transmission electron microscopy (HAADF STEM) mode in the angular range of ±60° at an increment of 1° at the KAIST Analysis Center for Research Advancement (KARA). Here, we deliberately reduced the electron beam dose with a total screen current of 0.23 nA, which is 10 times lower than the commonly used conditions but sufficient to obtain tomographic images without damaging Pt@CeO_2. To confirm whether or not there were structural changes by an electron beam, we checked projection images at a 0° before and after the acquisition of the tilt series and identified that structural evolution did not appear during the data collection. To resolve a linear stage drift at each angle while acquiring the STEM tilt series,

Please cite this article in press as: Lee et al., A measure of active interfaces in supported catalysts for high-temperature reactions, Chem (2021), https://doi.org/10.1016/j.chempr.2021.11.024

we aligned the obtained images using FEI's software package, Inspect 3D, by correlating an individual image with a separate reference image. The cross-correlation function was computed through the Fourier transform of the image. This procedure proceeds with an iterative cross-correlation method to minimize errors in alignment (maximum shift of pixel < -1). The subsequent reconstruction processes were carried out using FEI Inspect 3D. For the reconstruction, the simultaneous iterative reconstruction technique (SIRT)[57] with 25 iterations was used. The elongation factor was calculated from the maximum tilt angle (α) as follows:[58]

$$e = \sqrt{\frac{\alpha + \sin\alpha\cos\alpha}{\alpha - \sin\alpha\cos\alpha}} \qquad \text{(Equation 1)}$$

The factor obtained from Equation 1 was 1.55 when $\alpha = 60°$. For an accurate image analysis and quantification process, the *Z* direction voxel size of the reconstructed sample was adjusted, taking into account the elongation coefficient. To check the impact of the limited tilt range in this study, we acquired another set of tomographic images in the angular range of $\pm 70°$ at an increment of 1°. Thereafter, we repeated the reconstruction process at 5° intervals from $\pm 50°$ to $\pm 70°$. From this process, the minimum tilt angle at which information loss by the limited tilt range does not become critical was identified, and that was the angular range of over $\pm$ 60°, confirming the quantitative interpretation was reliable in this study (Figure S29).

Segmentation process

In order to quantify the significant morphological features of size-tunable catalysts, a segmentation process of designating each phase (Pt, Ceria, and pore) was utilized in a semi-automated manner. This approach proceeds with the use of a threshold with de-noising and contrast-enhanced filtering. The post-processing has shown its robustness throughout other tomography results.[59–63] To enhance the effect of the post-processing, background areas outside the region of interest (ROI) were removed by a binary mask. Through this process, only the Pt@CeO_2 catalyst remains, with the other pixels set to zero. Then, image de-noising was conducted using an anisotropic diffusion filter.[64] This reduces the noise without diluting the intensity of the edges. Anisotropic diffusion filtering is known as an effective tool for de-noising and edge preservation.[65–67] This process is essential to minimize the subjectivity of the analyst, and it can help to clarify the phase distinction after tomography and increase the accuracy of the quantification result. We checked the de-noising and the filtering effect on the quantification in Figure S30. Designation of the phase was performed using the Watershed segmentation algorithm.[68] This algorithm computes the gradient of the voxel and considers it as a 2D or 3D landscape. In order to distinguish each phase from the contour of the Pt NPs more precisely, adaptive histogram equalization filtering was used.[69] This process enhances the contrast between phases and makes it easier to distinguish between the pores and solid phase.

Quantification process

Based on the segmented data, the morphological features of the catalyst, including the particle diameter, 2PB and 3PB, were quantified with an Avizo Fire device (FEI Company). The calculated values are summarized in Table S2. To quantify the diameter of Pt NPs and the EMSA, the phase volume and surface area were calculated by converting the surface of the specific phase voxel into a triangular mesh. This method is a more accurate approach for calculating a 3D surface compared with a voxel counting algorithm. From the quantified surface area and volume of spherical Pt NPs, the particle size can be determined by the Brunauer-Emmett-Teller (BET) formula, $D = 6 \times V/S$.[70,71] To calculate the 3PB length, the voxels intersected with three

Please cite this article in press as: Lee et al., A measure of active interfaces in supported catalysts for high-temperature reactions, Chem (2021), https://doi.org/10.1016/j.chempr.2021.11.024

phases (Pt, ceria, and pore phase) were extracted. The 3PB length was calculated by extracting all voxels in contact with Pt, ceria, and the pore. The extracted voxels were "skeletonize"[72] to obtain their length, and the total length was divided by the mass of the Pt particle to yield the 3PB site density.

3D resolution estimation

The spatial resolution of the reconstructed sample was estimated using the FSC with a criterion of 0.143,[73,74] which correlates the reciprocal-space densities of the two sub-tomograms. For this purpose, the tilt series images were separated into two groups based on odd or even numbers of the order of the tilt angles. Each group was independently reconstructed, and their 3D volumes were used to compute the FSC curves as a function of the spatial frequency in the Fourier space. The resolution was determined as the value at which the FSC curve intersected with the pre-established threshold criterion. The resolution estimation process was performed in Matlab using an in-house code.

Simulated 3D tomography

Simulated 3D tomograms of the porous structure were prepared as follows. We generated 3D model volumes as ground truths. The size of each 3D model volume was 350 × 350 × 350 voxels with a voxel size of 0.3 nm. Each 3D model volume consists of a big sphere of 60 nm diameter that contains seven pores, with one pore at the origin and the other six symmetrically distributed at positions 6 nm away from the origin. We generated three such 3D model volumes with pore diameters of 1.5, 2.1, and 3.3 nm, respectively. Three tilt series with tilt angles ranging from -60° to 60° with 1° step were generated by taking linear forward-projections from the 3D model volumes. Each tilt series contains 121 projections; whose size was 350 × 350 pixels, with a pixel size of 0.3 nm. To properly simulate the experimental conditions, Poisson noise, random translation errors up to ± 0.45 nm, and random tilt angle errors up to $\pm 0.1^{\circ}$ were added to the tilt series. 3D tomograms were reconstructed from the generated tilt series and tilt angles using SIRT algorithm[71] with 30 iterations. To measure the diameters of pores in the simulated 3D tomogram, we first separated the 3D volume into two parts (the big sphere and pores). To designate each part, a segmentation process similar to that applied to Pt@CeO_2 catalysts was used in an automated manner. Next, the pore size was determined by assuming each pore as a spherical particle, and calculating the diameter can be estimated as $D = \sqrt[3]{\frac{6\times\ volume}{\pi}}$. The resolutions of the simulated 3D tomograms were estimated using the 0.143 criterion of the FSC analysis.[73,74]

Density functional theory calculations

We modeled the CeO_2(100) surface using a 3 × 3 supercell with three O–Ce–O triple layers. Quality test results confirmed that two key energy values, the oxygen vacancy formation energy from the 3PB and the oxygen binding energy on the 2PB, were well described using our supercell compared with a larger supercell, (5 × 5). A Pt NP composed of nine atoms was supported on the optimized CeO_2(100) substrate and repeatedly optimized upon the sequential adsorption of of six oxygen atoms to describe the catalyst structure under the CH_4 oxidation conditions. The bottom ceria triple-layer structure was fixed during all calculations to ensure structural robustness. An inverse Ce_7O_{14}/Pt(111) model was constructed by optimizing a Ce_7O_{14} cluster on a 7 × 7 × 4 Pt(111) slab (Figure S31). The supplemental information (Figures S32 and S33) section provides information about the CH_4 oxidation pathways and corresponding energetics calculated from the Ce_7O_{14}/Pt(111) model. We performed spin-polarized DFT calculations using a plane-wave basis with the

Please cite this article in press as: Lee et al., A measure of active interfaces in supported catalysts for high-temperature reactions, Chem (2021), https://doi.org/10.1016/j.chempr.2021.11.024

vienna ab-initio simulation package (VASP) code[75] and the Perdew-Burke-Ernzerhof (PBE) functional[76]. The DFT+U[77] scheme with U_{eff} = 5 eV[78] was applied for Ce ions to consider the localized Ce-*f* orbitals appropriately. The interaction between the ionic core and the valence electrons was described by the projector augmented wave method.[79] Valance electron wave functions were expanded in a plane-wave basis up to an energy cutoff of 400 eV. The Brillouin zone was sampled at the Γ-point for all calculations. The convergence criteria for the electronic structure and the atomic geometry were 10^{-4} eV and 0.03 eV/Å, respectively. We used a Gaussian smearing function with a finite temperature width of 0.05 eV in order to improve the convergence of states near the Fermi level. The location and energy of transition states (TSs) were calculated with the climbing-image nudged-elastic-band method.[80]

SUPPLEMENTAL INFORMATION

Supplemental information can be found online at https://doi.org/10.1016/j.chempr.2021.11.024.

ACKNOWLEDGMENTS

S.L., S.K., J.H.K., J.S., and W.J. were supported financially by grants from the National Research Foundation of Korea (NRF) and the KAIST Institute of Technology Value Creation, Industry Liaison Center (G-CORE Project) funded by the Korean Government (MSIT) (NRF-2017M3A7B4049547, NRF-2019R1A2C2006006, NRF-2021M3H4A1A01002695, and N11210015). H.H., H.C., and H.Y.K. were supported financially by a grant from the National Research Foundation of Korea (NRF) funded by the Korean Government (MSIT) (NRF-2019R1A2C1089256). H.Y.K. thanks the support from the Basic Science Research Program through the NRF funded by the Ministry of Education (2021R1A6A1A03043682). K.T.B. and K.T.L. were supported financially by grants from the National Research Foundation of Korea (NRF) funded by the Korean Government (MSIT) (NRF-2019M3E6A1103944, NRF-2020R1A2C2010690, and NRF-2021M3H4A1A01002695). J.L. and Y.Y. were supported by the National Research Foundation of Korea (NRF) grant funded by the Korean Government (MSIT) (no. 2020R1C1C100623911). J.L. was also partially supported by the KAIST-funded Global Singularity Research Program (M3I3) for 2021. This research used the resources of the Center for Functional Nanomaterials, which is a U.S. DOE Office of Science Facility, and the Scientific Data and Computing Center, a component of the Computational Science Initiative, at Brookhaven National Laboratory (contract no. DE-SC0012704). The National Institute of Supercomputing and the Network/Korea Institute of Science and Technology Information (KSC-2019-CRE-0210) also provided computing time. This research was supported by KAIST Institute for the NanoCentury.

AUTHOR CONTRIBUTIONS

S.L. and W.J. conceived of the idea for this study. S.L. prepared and characterized the catalysts. H.H. and H.C. performed the DFT calculations. K.T.B. conducted the reconstruction and quantification of the catalysts. S.K. synthesized the Pt@SiO_2 catalysts and collected the associated activity data. J.L. and Y.Y. designed and performed the simulated 3D tomogram experiments. J.H.K. and J.S. assisted in the preparation of the catalysts. J.S.C. supported collecting TEM data for tomography. Y.-R.J. and B.-J.K. supported collecting *in situ* TEM data. W.J., H.Y.K., and K.T.L. supervised the project and wrote the manuscript, and all authors commented on the data and the manuscript. S.L., H.H., and K.T.B. equally contributed to this work.

DECLARATION OF INTERESTS

The authors declare no competing interests.

Received: April 30, 2021
Revised: August 4, 2021
Accepted: November 25, 2021
Published: December 23, 2021

REFERENCES

1. Kattel, S., Ramírez, P.J., Chen, J.G., Rodriguez, J.A., and Liu, P. (2017). Active sites for CO_2 hydrogenation to methanol on Cu/ZnO catalysts. Science *355*, 1296–1299. https://doi.org/10.1126/science.aal3573.

2. Choi, Y., Cha, S.K., Ha, H., Lee, S., Seo, H.K., Lee, J.Y., Kim, H.Y., Kim, S.O., and Jung, W. (2019). Unravelling inherent electrocatalysis of mixed-conducting oxide activated by metal nanoparticle for fuel cell electrodes. Nat. Nanotechnol. *14*, 245–251. https://doi.org/10.1038/s41565-019-0367-4.

3. Farmer, J.A., and Campbell, C.T. (2010). Ceria maintains smaller metal catalyst particles by strong metal-support bonding. Science *329*, 933–936. https://doi.org/10.1126/science.1191778.

4. Kwak, N.W., Jeong, S.J., Seo, H.G., Lee, S., Kim, Y.J., Kim, J.K., Byeon, P., Chung, S.-Y., and Jung, W.C. (2018). *In situ* synthesis of supported metal nanocatalysts through heterogeneous doping. Nat. Commun. *9*, 4829. https://doi.org/10.1038/s41467-018-07050-y.

5. Jo, Y.-R., Koo, B., Seo, M.-J., Kim, J.K., Lee, S., Kim, K., Han, J.W., Jung, W., and Kim, B.-J. (2019). Growth kinetics of individual Co particles ex-solved on $SrTi_{0.75}Co_{0.25}O_{3-\delta}$ polycrystalline perovskite thin films. J. Am. Chem. Soc. *141*, 6690–6697. https://doi.org/10.1021/jacs.9b01882.

6. Fu, Q., Weber, A., and Flytzani-Stephanopoulos, M. (2001). Nanostructured Au–CeO_2 catalysts for low-temperature water-gas shift. Catal. Lett. *77*, 87–95. https://doi.org/10.1023/A:1012666128812.

7. Rodriguez, J.A., Ma, S., Liu, P., Hrbek, J., Evans, J., and Pérez, M. (2007). Activity of CeO_x and TiO_x nanoparticles grown on Au(111) in the water-gas shift reaction. Science *318*, 1757–1760. https://doi.org/10.1126/science.1150038.

8. Green, I.X., Tang, W.J., Neurock, M., and Yates, J.T. (2011). Spectroscopic observation of dual catalytic sites during oxidation of CO on a Au/TiO_2 catalyst. Science *333*, 736–739. https://doi.org/10.1126/science.1207272.

9. Park, J.B., Graciani, J., Evans, J., Stacchiola, D., Senanayake, S.D., Barrio, L., Liu, P., Sanz, J.F., Hrbek, J., and Rodriguez, J.A. (2010). Gold, copper, and platinum nanoparticles dispersed on CeO_x/TiO_2(110) surfaces: high water-gas shift activity and the nature of the mixed-metal oxide at the nanometer level. J. Am. Chem. Soc. *132*, 356–363. https://doi.org/10.1021/ja9087677.

10. Kim, K., Yoo, J.D., Lee, S., Bae, M., Bae, J., Jung, W.C., and Han, J.W. (2017). A simple descriptor to rapidly screen CO oxidation activity on rare-earth metal-doped CeO_2: from experiment to first-principles. ACS Appl. Mater. Interfaces *9*, 15449–15458. https://doi.org/10.1021/acsami.7b01844.

11. Kayaalp, B., Lee, S., Klauke, K., Seo, J., Nodari, L., Kornowski, A., Jung, W., and Mascotto, S. (2019). Template-free mesoporous $La_{0.3}Sr_{0.7}Fe_xTi_{1-x}O_{3\pm\delta}$ for CH_4 and CO oxidation catalysis. Appl. Catal. B *245*, 536–545. https://doi.org/10.1016/j.apcatb.2018.12.077.

12. Montini, T., Melchionna, M., Monai, M., and Fornasiero, P. (2016). Fundamentals and catalytic applications of CeO_2-based materials. Chem. Rev. *116*, 5987–6041. https://doi.org/10.1021/acs.chemrev.5b00603.

13. Rodriguez, J.A., Grinter, D.C., Liu, Z.Y., Palomino, R.M., and Senanayake, S.D. (2017). Ceria-based model catalysts: fundamental studies on the importance of the metal-ceria interface in CO oxidation, the water-gas shift, CO_2 hydrogenation, and methane and alcohol reforming. Chem. Soc. Rev. *46*, 1824–1841. https://doi.org/10.1039/c6cs00863a.

14. Sun, C.W., Li, H., and Chen, L.Q. (2012). Nanostructured ceria-based materials: synthesis, properties, and applications. Energy Environ. Sci. *5*, 8475–8505. https://doi.org/10.1039/c2ee22310d.

15. An, K., Alayoglu, S., Musselwhite, N., Plamthottam, S., Melaet, G., Lindeman, A.E., and Somorjai, G.A. (2013). Enhanced CO oxidation rates at the interface of mesoporous oxides and Pt nanoparticles. J. Am. Chem. Soc. *135*, 16689–16696. https://doi.org/10.1021/ja4088743.

16. Kayaalp, B., Lee, S., Nodari, L., Seo, J., Kim, S., Jung, W., and Mascotto, S. (2020). Pt nanoparticles supported on a mesoporous $(La,Sr)(Ti,Fe)O_{3-\delta}$ solid solution for the catalytic oxidation of CO and CH_4. ACS Appl. Nano Mater. *3*, 11352–11362. https://doi.org/10.1021/acsanm.0c02456.

17. Chen, A.L., Yu, X.J., Zhou, Y., Miao, S., Li, Y., Kuld, S., Sehested, J., Liu, J.Y., Aoki, T., Hong, S., et al. (2019). Structure of the catalytically active copper–ceria interfacial perimeter. Nat. Catal. *2*, 334–341. https://doi.org/10.1038/s41929-019-0226-6.

18. Pereira-Hernández, X.I., DeLaRiva, A., Muravev, V., Kunwar, D., Xiong, H., Sudduth, B., Engelhard, M., Kovarik, L., Hensen, E.J.M., Wang, Y., and Datye, A.K. (2019). Tuning Pt–CeO_2 interactions by high-temperature vapor-phase synthesis for improved reducibility of lattice oxygen. Nat. Commun. *10*, 1358. https://doi.org/10.1038/s41467-019-09308-5.

19. Daelman, N., Capdevila-Cortada, M., and López, N. (2019). Dynamic charge and oxidation state of Pt/CeO_2 single-atom catalysts. Nat. Mater. *18*, 1215–1221. https://doi.org/10.1038/s41563-019-0444-y.

20. Yao, S., Zhang, X., Zhou, W., Gao, R., Xu, W.Q., Ye, Y., Lin, L., Wen, X., Liu, P., Chen, B., et al. (2017). Atomic-layered Au clusters on α-MoC as catalysts for the low-temperature water-gas shift reaction. Science *357*, 389–393. https://doi.org/10.1126/science.aah4321.

21. Nie, L., Mei, D.H., Xiong, H.F., Peng, B., Ren, Z.B., Hernandez, X.I.P., DeLaRiva, A., Wang, M., Engelhard, M.H., Kovarik, L., et al. (2017). Activation of surface lattice oxygen in single-atom Pt/CeO_2 for low-temperature CO oxidation. Science *358*, 1419–1423. https://doi.org/10.1126/science.aao2109.

22. van Deelen, T.W., Hernández Mejía, C., and de Jong, K.P. (2019). Control of metal-support interactions in heterogeneous catalysts to enhance activity and selectivity. Nat. Catal. *2*, 955–970. https://doi.org/10.1038/s41929-019-0364-x.

23. Yoo, M., Yu, Y.-S., Ha, H., Lee, S., Choi, J.-S., Oh, S., Kang, E., Choi, H., An, H., Lee, K.-S., et al. (2020). A tailored oxide interface creates dense Pt single-atom catalysts with high catalytic activity. Energy Environ. Sci. *13*, 1231–1239. https://doi.org/10.1039/C9EE03492G.

24. Lee, S., Lin, C., Kim, S., Mao, X., Kim, T., Kim, S.-J., Gorte, R.J., and Jung, W. (2021). Manganese oxide overlayers promote CO oxidation on Pt. ACS Catal *11*, 13935–13946. https://doi.org/10.1021/acscatal.1c04214.

25. Bruix, A., Rodriguez, J.A., Ramírez, P.J., Senanayake, S.D., Evans, J., Park, J.B., Stacchiola, D., Liu, P., Hrbek, J., and Illas, F. (2012). A new type of strong metal-support interaction and the production of H_2 through the transformation of water on Pt/CeO_2(111) and Pt/CeO_x/TiO_2(110) catalysts. J. Am. Chem. Soc. *134*, 8968–8974. https://doi.org/10.1021/ja302070k.

26. Vayssilov, G.N., Lykhach, Y., Migani, A., Staudt, T., Petrova, G.P., Tsud, N., Skála, T., Bruix, A., Illas, F., Prince, K.C., et al. (2011). Support nanostructure boosts oxygen transfer to catalytically active platinum nanoparticles. Nat. Mater. *10*, 310–315. https://doi.org/10.1038/nmat2976.

27. Foppa, L., Margossian, T., Kim, S.M., Müller, C., Copéret, C., Larmier, K., and Comas-Vives, A. (2017). Contrasting the role of Ni/Al_2O_3 interfaces in water-gas shift and dry reforming

Please cite this article in press as: Lee et al., A measure of active interfaces in supported catalysts for high-temperature reactions, Chem (2021), https://doi.org/10.1016/j.chempr.2021.11.024

of methane. J. Am. Chem. Soc. *139*, 17128–17139. https://doi.org/10.1021/jacs.7b08984.

28. Liu, Z.Y., Lustemberg, P., Gutiérrez, R.A., Carey, J.J., Palomino, R.M., Vorokhta, M., Grinter, D.C., Ramírez, P.J., Matolín, V., Nolan, M., et al. (2017). *In situ* investigation of methane dry reforming on metal/ceria(111) surfaces: metal-support interactions and C–H bond activation at low temperature. Angew. Chem. Int. Ed. Engl. *56*, 13041–13046. https://doi.org/10.1002/anie.201707538.

29. Corral-Pérez, J.J., Bansode, A., Praveen, C.S., Kokalj, A., Reymond, H., Comas-Vives, A., VandeVondele, J., Copéret, C., von Rohr, P.R., and Urakawa, A. (2018). Decisive role of perimeter sites *in silica*-supported Ag nanoparticles in selective dydrogenation of CO_2 to methyl formate in the presence of methanol. J. Am. Chem. Soc. *140*, 13884–13891. https://doi.org/10.1021/jacs.8b08505.

30. Liu, A.N., Liu, X., Liu, L.C., Pu, Y., Guo, K., Tan, W., Gao, S., Luo, Y.D., Yu, S.H., Si, R., et al. (2019). Getting insights into the temperature-specific active sites on platinum nanoparticles for CO oxidation: a combined *in situ* spectroscopic and *ab initio* density functional theory study. ACS Catal *9*, 7759–7768. https://doi.org/10.1021/acscatal.9b02552.

31. Suchorski, Y., Kozlov, S.M., Bespalov, I., Datler, M., Vogel, D., Budinska, Z., Neyman, K.M., and Rupprechter, G. (2018). The role of metal/oxide interfaces for long-range metal particle activation during CO oxidation. Nat. Mater. *17*, 519–522. https://doi.org/10.1038/s41563-018-0080-y.

32. Hanukovich, S., Dang, A., and Christopher, P. (2019). Influence of metal oxide support acid sites on Cu-catalyzed nonoxidative dehydrogenation of ethanol to acetaldehyde. ACS Catal *9*, 3537–3550. https://doi.org/10.1021/acscatal.8b05075.

33. Gänzler, A.M., Casapu, M., Maurer, F., Störmer, H., Gerthsen, D., Ferré, G., Vernoux, P., Bornmann, B., Frahm, R., Murzin, V., et al. (2018). Tuning the Pt/CeO_2 interface by *in situ* variation of the Pt particle size. ACS Catal *8*, 4800–4811. https://doi.org/10.1021/acscatal.8b00330.

34. Murata, K., Eleeda, E., Ohyama, J., Yamamoto, Y., Arai, S., and Satsuma, A. (2019). Identification of active sites in CO oxidation over a Pd/Al_2O_3 catalyst. Phys. Chem. Chem. Phys. *21*, 18128–18137. https://doi.org/10.1039/c9cp03943k.

35. Cargnello, M., Doan-Nguyen, V.V.T., Gordon, T.R., Diaz, R.E., Stach, E.A., Gorte, R.J., Fornasiero, P., and Murray, C.B. (2013). Control of metal nanocrystal size reveals metal-support interface role for ceria catalysts. Science *341*, 771–773. https://doi.org/10.1126/science.1240148.

36. Hansen, T.W., DeLaRiva, A.T., Challa, S.R., and Datye, A.K. (2013). Sintering of catalytic nanoparticles: particle migration or ostwald ripening? Acc. Chem. Res. *46*, 1720–1730. https://doi.org/10.1021/ar3002427.

37. Cargnello, M., Delgado Jaén, J.J., Hernández Garrido, J.C., Bakhmutsky, K., Montini, T., Calvino Gámez, J.J., Gorte, R.J., and Fornasiero, P. (2012). Exceptional activity for methane combustion over modular Pd@CeO_2 subunits on functionalized Al_2O_3. Science *337*, 713–717. https://doi.org/10.1126/science.1222887.

38. Zhang, F., Liu, Z.Y., Zhang, S.H., Akter, N., Palomino, R.M., Vovchok, D., Orozco, I., Salazar, D., Rodriguez, J.A., Llorca, J., et al. (2018). *In situ* elucidation of the active state of Co–CeO_x catalysts in the dry reforming of methane: the important role of the reducible oxide support and interactions with cobalt. ACS Catal *8*, 3550–3560. https://doi.org/10.1021/acscatal.7b03640.

39. Seo, J., Lee, S., Koo, B., and Jung, W. (2018). Controlling the size of Pt nanoparticles with a cationic surfactant, C_nTABr. CrystEngComm *20*, 2010–2015.

40. Lee, S., Seo, J., and Jung, W. (2016). Sintering-resistant Pt@CeO_2 nanoparticles for high-temperature oxidation catalysis. Nanoscale *8*, 10219–10228. https://doi.org/10.1039/c6nr00170j.

41. Joo, S.H., Park, J.Y., Tsung, C.-K., Yamada, Y., Yang, P.D., and Somorjai, G.A. (2009). Thermally stable Pt/mesoporous silica core-shell nanocatalysts for high-temperature reactions. Nat. Mater. *8*, 126–131. https://doi.org/10.1038/nmat2329.

42. Kim, S., Lee, S., and Jung, W. (2019). Sintering resistance of Pt@SiO_2 core-shell catalyst. ChemCatChem *11*, 4653–4659. https://doi.org/10.1002/cctc.201900934.

43. Wang, Z.L. (2000). Transmission electron microscopy of shape-controlled nanocrystals and their assemblies. J. Phys. Chem. B *104*, 1153–1175. https://doi.org/10.1021/jp993593c.

44. Zhang, S., Chen, C., Cargnello, M., Fornasiero, P., Gorte, R.J., Graham, G.W., and Pan, X. (2015). Dynamic structural evolution of supported palladium–ceria core-shell catalysts revealed by *in situ* electron microscopy. Nat. Commun. *6*, 7778. https://doi.org/10.1038/ncomms8778.

45. Jones, J., Xiong, H., DeLaRiva, A.T., Peterson, E.J., Pham, H., Challa, S.R., Qi, G., Oh, S., Wiebenga, M.H., Pereira Hernández, X.I., et al. (2016). Thermally stable single-atom platinum-on-ceria catalysts via atom trapping. Science *353*, 150–154. https://doi.org/10.1126/science.aaf8800.

46. Kunwar, D., Zhou, S., DeLaRiva, A., Peterson, E.J., Xiong, H., Pereira-Hernández, X.I., Purdy, S.C., ter Veen, R., Brongersma, H.H., Miller, J.T., et al. (2019). Stabilizing high metal loadings of thermally stable platinum single atoms on an industrial catalyst support. ACS Catal *9*, 3978–3990. https://doi.org/10.1021/acscatal.8b04885.

47. Klug, A., and Crowther, R.A. (1972). Three-dimensional image reconstruction from the viewpoint of information theory. Nature *238*, 435–440. https://doi.org/10.1038/238435a0.

48. Riscoe, A.R., Wrasman, C.J., Herzing, A.A., Hoffman, A.S., Menon, A., Boubnov, A., Vargas, M., Bare, S.R., and Cargnello, M. (2019). Transition state and product diffusion control by polymer-nanocrystal hybrid catalysts. Nat. Catal. *2*, 852–863. https://doi.org/10.1038/s41929-019-0322-7.

49. Nguyen, T.S., McKeever, P., Arredondo-Arechavala, M., Wang, Y.-C., Slater, T.J.A., Haigh, S.J., Beale, A.M., and Thompson, J.M. (2020). Correlation of the ratio of metallic to oxide species with activity of PdPt catalysts for methane oxidation. Catal. Sci. Technol. *10*, 1408–1421. https://doi.org/10.1039/C9CY02371B.

50. Tao, F.F., Shan, J.-J., Nguyen, L., Wang, Z.Y., Zhang, S.R., Zhang, L., Wu, Z.L., Huang, W.X., Zeng, S.B., and Hu, P. (2015). Understanding complete oxidation of methane on spinel oxides at a molecular level. Nat. Commun. *6*, 7798. https://doi.org/10.1038/ncomms8798.

51. Arai, H., Yamada, T., Eguchi, K., and Seiyama, T. (1986). Catalytic combustion of methane over various perovskite-type oxides. Appl. Catal. *26*, 265–276. https://doi.org/10.1016/S0166-9834(00)82556-7.

52. Yao, Y.-F.Y. (1980). Oxidation of alkanes over noble-metal catalysts. Ind. Eng. Chem. Prod. Res. Dev. *19*, 293–298. https://doi.org/10.1021/i360075a003.

53. Wang, X., and Gorte, R.J. (2002). A study of steam reforming of hydrocarbon fuels on Pd/ceria. Appl. Catal. A *224*, 209–218. https://doi.org/10.1016/S0926-860X(01)00783-9.

54. Tang, W., Hu, Z.P., Wang, M.J., Stucky, G.D., Metiu, H., and McFarland, E.W. (2010). Methane complete and partial oxidation catalyzed by Pt-doped CeO2. J. Catal. *273*, 125–137. https://doi.org/10.1016/j.jcat.2010.05.005.

55. Lustemberg, P.G., Ramírez, P.J., Liu, Z.Y., Gutiérrez, R.A., Grinter, D.G., Carrasco, J., Senanayake, S.D., Rodriguez, J.A., and Ganduglia-Pirovano, M.V. (2016). Room-temperature activation of methane and dry re-forming with CO_2 on Ni-CeO_2(111) surfaces: effect of Ce^{3+} sites and metal-support interactions on C–H bond cleavage. ACS Catal *6*, 8184–8191. https://doi.org/10.1021/acscatal.6b02360.

56. Chin, Y.-H., Buda, C., Neurock, M., and Iglesia, E. (2011). Reactivity of chemisorbed oxygen atoms and their catalytic consequences during CH_4–O_2 catalysis on supported Pt clusters. J. Am. Chem. Soc. *133*, 15958–15978. https://doi.org/10.1021/ja202411v.

57. Holzer, L., Indutnyi, F., Gasser, P.H., Münch, B., and Wegmann, M. (2004). Three-dimensional analysis of porous $BaTiO_3$ ceramics using FIB nanotomography. J. Microsc. *216*, 84–95. https://doi.org/10.1111/j.0022-2720.2004.01397.x.

58. Zhou, J., Yang, Y., Yang, Y., Kim, D.S., Yuan, A., Tian, X., Ophus, C., Sun, F., Schmid, A.K., Nathanson, M., et al. (2019). Observing crystal nucleation in four dimensions using atomic electron tomography. Nature *570*, 500–503. https://doi.org/10.1038/s41586-019-1317-x.

59. Xu, R., Chen, C.-C., Wu, L., Scott, M.C., Theis, W., Ophus, C., Bartels, M., Yang, Y., Ramezani-Dakhel, H., Sawaya, M.R., et al. (2015). Three-dimensional coordinates of individual atoms in materials revealed by electron tomography. Nat. Mater. *14*, 1099–1103. https://doi.org/10.1038/nmat4426.

60. Lopez-Haro, M., Guétaz, L., Printemps, T., Morin, A., Escribano, S., Jouneau, P.-H., Bayle-Guillemaud, P., Chandezon, F., and Gebel, G. (2014). Three-dimensional analysis of nafion

Please cite this article in press as: Lee et al., A measure of active interfaces in supported catalysts for high-temperature reactions, Chem (2021), https://doi.org/10.1016/j.chempr.2021.11.024

layers in fuel cell electrodes. Nat. Commun. *5*, 5229. https://doi.org/10.1038/ncomms6229.

61. Zečević, J., Gommes, C.J., Friedrich, H., de Jongh, P.E., and de Jong, K.P. (2012). Mesoporosity of zeolite Y: quantitative three-dimensional study by image analysis of electron tomograms. Angew. Chem. Int. Ed. Engl. *51*, 4213–4217. https://doi.org/10.1002/anie.201200317.

62. Gommes, C.J., de Jong, K., Pirard, J.-P., and Blacher, S. (2005). Assessment of the 3D localization of metallic nanoparticles in Pd/SiO_2 cogelled catalysts by electron tomography. Langmuir *21*, 12378–12385. https://doi.org/10.1021/la051682c.

63. Yates, T.J.V., Thomas, J.M., Fernandez, J.-J., Terasaki, O., Ryoo, R., and Midgley, P.A. (2006). Three-dimensional real-space crystallography of MCM-48 mesoporous silica revealed by scanning transmission electron tomography. Chem. Phys. Lett. *418*, 540–543. https://doi.org/10.1016/j.cplett.2005.11.031.

64. Ward, E.P.W., Yates, T.J.V., Fernández, J.-J., Vaughan, D.E.W., and Midgley, P.A. (2007). Three-dimensional nanoparticle distribution and local curvature of heterogeneous catalysts revealed by electron tomography. J. Phys. Chem. C *111*, 11501–11505. https://doi.org/10.1021/jp072441b.

65. Prieto, G., Zečević, J., Friedrich, H., de Jong, K.P., and de Jongh, P.E. (2013). Towards stable catalysts by controlling collective properties of supported metal nanoparticles. Nat. Mater. *12*, 34–39. https://doi.org/10.1038/nmat3471.

66. Goris, B., De Beenhouwer, J., De Backer, A., Zanaga, D., Batenburg, K.J., Sánchez-Iglesias, A., Liz-Marzán, L.M., Van Aert, S., Bals, S., Sijbers, J., and Van Tendeloo, G. (2015). Measuring lattice strain in three dimensions through electron microscopy. Nano Lett *15*, 6996–7001. https://doi.org/10.1021/acs.nanolett.5b03008.

67. Haberfehlner, G., Thaler, P., Knez, D., Volk, A., Hofer, F., Ernst, W.E., and Kothleitner, G. (2015). Formation of bimetallic clusters in superfluid helium nanodroplets analysed by atomic resolution electron tomography. Nat. Commun. *6*, 8779. https://doi.org/10.1038/ncomms9779.

68. Saha, P.K., Borgefors, G., and di Baja, G.S. (2016). A survey on skeletonization algorithms and their applications. Pattern Recognit. Lett. *76*, 3–12. https://doi.org/10.1016/j.patrec.2015.04.006.

69. Brunauer, S., Emmett, P.H., and Teller, E. (1938). Adsorption of gases in multimolecular layers. J. Am. Chem. Soc. *60*, 309–319. https://doi.org/10.1021/ja01269a023.

70. Gilbert, P. (1972). Iterative methods for the three-dimensional reconstruction of an object from projections. J. Theor. Biol. *36*, 105–117. https://doi.org/10.1016/0022-5193(72)90180-4.

71. Pizer, S.M., Amburn, E.P., Austin, J.D., Cromartie, R., Geselowitz, A., Greer, T., ter Haar Romeny, B., Zimmerman, J.B., and Zuiderveld, K. (1987). Adaptive histogram equalization and its variations. Comput. Vis. Graph. Image Process. *39*, 355–368. https://doi.org/10.1016/S0734-189X(87)80186-X.

72. van Heel, M., and Schatz, M. (2005). Fourier shell correlation threshold criteria. J. Struct. Biol. *151*, 250–262. https://doi.org/10.1016/j.jsb.2005.05.009.

73. Nieuwenhuizen, R.P.J., Lidke, K.A., Bates, M., Puig, D.L., Grünwald, D., Stallinga, S., and Rieger, B. (2013). Measuring image resolution in optical nanoscopy. Nat. Methods *10*, 557–562. https://doi.org/10.1038/nmeth.2448.

74. Kresse, G., and Furthmüller, J. (1996). Efficiency of *ab-initio* total energy calculations for metals and semiconductors using a plane-wave basis set. Comput. Mater. Sci. *6*, 15–50. https://doi.org/10.1016/0927-0256(96)00008-0.

75. Perdew, J.P., Burke, K., and Ernzerhof, M. (1996). Generalized gradient approximation made simple. Phys. Rev. Lett. *77*, 3865–3868. https://doi.org/10.1103/PhysRevLett.77.3865.

76. Dudarev, S.L., Botton, G.A., Savrasov, S.Y., Humphreys, C.J., and Sutton, A.P. (1998). Electron-energy-loss spectra and the structural stability of nickel oxide: an LSDA+U study. Phys. Rev. B *57*, 1505–1509. https://doi.org/10.1103/PhysRevB.57.1505.

77. Kim, H.Y., Lee, H.M., and Henkelman, G. (2012). CO oxidation mechanism on CeO_2-supported Au nanoparticles. J. Am. Chem. Soc. *134*, 1560–1570. https://doi.org/10.1021/ja207510v.

78. Blöchl, P.E. (1994). Projector augmented-wave method. Phys. Rev. B *50*, 17953–17979. https://doi.org/10.1103/PhysRevB.50.17953.

79. Henkelman, G., Uberuaga, B.P., and Jónsson, H. (2000). A climbing image nudged elastic band method for finding saddle points and minimum energy paths. J. Chem. Phys. *113*, 9901–9904. https://doi.org/10.1063/1.1329672.

80. Vincent, L., and Soille, P. (1991). Watersheds in digital spaces: an efficient algorithm based on immersion simulations. IEEE Trans. Pattern Anal. Mach. Intell. *13*, 583–598. https://doi.org/10.1109/34.87344.